

# Addendum II to Proposal P36

## **Systematic Error Analysis of the Measurement of $\Gamma(K^+ \rightarrow e^+\nu)/\Gamma(K^+ \rightarrow \mu^+\nu)$**

P36 collaboration

December 27, 2011

### **Abstract**

In this report we present the revised systematic error analysis for the lepton-universality measurement in the P36 experiment. It was confirmed that the total size of the relative systematic uncertainty is  $1.5 \times 10^{-3}$  for  $R_K$  rendering this experiment feasible to test the lepton universality with the sensitivity of  $\Delta R_K/R_K = 2.5 \times 10^{-3}$ . The methods to evaluate the  $K_{e2}/K_{\mu2}$  acceptance ratio by means of experimental data are also discussed.

# Contents

<b>1</b>	<b>Introduction</b>	<b>4</b>
<b>2</b>	<b>Principle of the experiment and sources of systematic errors</b>	<b>5</b>
<b>3</b>	<b>Estimate of the <math>K_{e2}/K_{\mu2}</math> acceptance ratio</b>	<b>7</b>
3.1	$K_{e2}/K_{\mu2}$ acceptance ratio as a direct source of a systematic error . . .	7
3.2	Factors contributing to the acceptance ratio . . . . .	10
3.3	Estimate of the spectrometer acceptance . . . . .	10
3.3.1	Pure Monte Carlo simulation . . . . .	10
3.3.2	Estimate with the help of $K_{\mu2}$ peak . . . . .	12
3.3.3	Estimate with the help of $K_{\mu3}$ spectrum . . . . .	14
3.3.4	Estimate by the E246 $K_{\mu3}$ data . . . . .	16
3.4	$e^+/\mu^+$ interactions in the target . . . . .	18
<b>4</b>	<b>Systematic errors from the measurement (1)</b>	
	– <b>Detector performance</b> –	<b>20</b>
4.1	Errors due to chamber inefficiency . . . . .	20
4.1.1	Tracking efficiency . . . . .	20
4.1.2	Efficiency measurement . . . . .	20
4.1.3	Tracking efficiency of $K_{e2}$ and $K_{\mu2}$ . . . . .	21
4.1.4	Error estimate . . . . .	22
4.1.5	Multiple scattering . . . . .	24
4.2	PID performance . . . . .	25
4.2.1	Anticipated performance of AC and TOF . . . . .	25
4.2.2	Addition of a Pb-glass counter for PID . . . . .	25
4.2.3	PID efficiency calibration . . . . .	27
4.3	CsI(Tl) inefficiency . . . . .	28
4.3.1	Effects on $K_{\mu2\gamma}$ . . . . .	29
4.3.2	Effects on $K_{e2\gamma}$ . . . . .	29
4.4	Trigger and DAQ . . . . .	30
<b>5</b>	<b>Systematic errors from the measurement (2)</b>	
	– <b>Errors due to due to backgrounds</b> –	<b>31</b>
5.1	In-flight $\mu^+$ decay . . . . .	31
5.2	$e^\pm$ creation from a radiated photon in $K^+ \rightarrow \mu^+ \nu \gamma$ decay . . . . .	32
5.3	Accidental beam halo hit in CsI(Tl) . . . . .	34
5.4	Accidental beam hits in the aerogel Cherenkov counters . . . . .	35
5.5	Accidental events due to the $K^+$ to $K^0$ conversion . . . . .	37
<b>6</b>	<b>Systematic errors from the measurement (3)</b>	
	– <b>Analysis</b> –	<b>38</b>
6.1	Analysis code and cut parameters . . . . .	38

6.2	Uncertainty of the SD component subtraction . . . . .	39
<b>7</b>	<b>Systematic errors in the MC simulation</b>	<b>42</b>
7.1	Acceptance estimate . . . . .	42
7.1.1	Acceptance . . . . .	42
7.1.2	Magnetic field . . . . .	43
7.2	Input parameters . . . . .	43
7.2.1	Effect of kaon stopping distribution ambiguity . . . . .	44
7.3	Interactions of emitted particles in the target . . . . .	45
7.3.1	Error due to decay vertex resolution . . . . .	46
7.3.2	Error due to material thickness uncertainty . . . . .	46
7.3.3	Error estimate . . . . .	48
7.3.4	Other materials outside the target and associated error . . . . .	49
7.4	Internal bremsstrahlung theory . . . . .	49
<b>8</b>	<b>Summary</b>	<b>51</b>
8.1	Summary of systematic error . . . . .	51
8.2	Control and calibration runs . . . . .	52
8.3	Conclusion . . . . .	52

# 1 Introduction

This report is an Addendum to the experimental proposal P36, “Measurement of  $\Gamma(K^+ \rightarrow e^+\nu)/\Gamma(K^+ \rightarrow \mu^+\nu)$  and search for heavy sterile neutrinos using the TREK detector system” [1]. We present a detailed and improved analysis of systematic errors in the search for lepton universality violation in  $K_{l2}$  decays in the P36 experiment. We submitted to the 11th PAC meeting the first Addendum [2]<sup>a)</sup> to the proposal describing the systematic-error estimate and some detector developments, and obtained a recommendation for stage-1 approval. However, it was regarded to be necessary to investigate systematic-error issues further with higher precision and reliability, considering the proposed high sensitivity of the measurement. Hence, we have now carefully reviewed all of the conceivable sources of the systematic errors, and completed an improved analysis, which we present in this report.

The  $K_{e2}$ -and  $K_{\mu2}$  acceptance ratio is one of the most essential factors in this experiment and we anticipate it to have the largest contribution to the systematic uncertainties. In Addendum I we discussed our expectation to suppress this uncertainty below  $10^{-3}$  by taking advantage of the Monte Carlo simulation code, which was used for the Toroidal detector setup in the previous E246/E470 KEK-PS experiment and whose validity has been well proven. In the course of the present systematic-error analysis refinement, however, we did establish methods to estimate the acceptance ratio by using experimental data, in some parts, and we could estimate the associated uncertainty. Our new result confirms our earlier expectation.

Other sources of systematic errors were also rechecked and refined in this report. It is important that all the potential sources are carefully investigated. Whereas we studied only the seemingly large-error sources in Addendum I, here we have also performed a systematic analysis covering the small ones. Hence, this report supersedes the systematic-error analysis of Addendum I.

In some parts of Addendum I, we gave only semi-quantitative discussions or methodology how to suppress and estimate the systematic errors. We have now performed analyses based on experimental data as much as possible. Also some descriptions were improved. For instance, the explanation of how to subtract the structure-dependent part (SD) of the radiative decays is now clearer and an improved estimate of the associated error is given.

After summarizing the experimental principle and classifying the sources of systematic errors in Section 2, we will discuss in Section 3 the methods to evaluate the ratio of the detector acceptance between  $K_{e2}$  and  $K_{\mu2}$  by using the experimental data, before going into detailed discussions of other systematic errors in Section 4-7. The summary table of the total systematic error (Section 8) is thus revised and the final sensitivity of the experiment is now updated.

---

<sup>a)</sup>Hereafter we denote it as “Addendum I” in this report.

## 2 Principle of the experiment and sources of systematic errors

We refer to the proposal [1] for a detailed discussion of the experimental principle. Here, only a brief summary is given with the experimental setup shown in Figure 1, the data analysis scheme in Figure 2, and a summary of experiment parameters given in Table 1. We search for “new physics” in the deviation of the decay-width ratio between the  $K_{e2}$  and  $K_{\mu2}$  decays from the standard model (SM) prediction. Since the counting rate  $N$  of  $K_{l2}$  decays is proportional to the decay width  $\Gamma$  and detector acceptance  $\Omega$  of each channel as  $N(K_{l2}) \propto \Gamma(K_{l2}) \times \Omega(K_{l2})$ , the ratio of the  $K_{e2}$  to  $K_{\mu2}$  decay widths can be expressed as:

$$R_K = \frac{\Gamma(K^+ \rightarrow e^+\nu)}{\Gamma(K^+ \rightarrow \mu^+\nu)} = N(\tilde{K}_{e2})/N(\tilde{K}_{\mu2}) \cdot \Omega(\tilde{K}_{\mu2})/\Omega(\tilde{K}_{e2}), \quad (1)$$

where  $N(\tilde{K}_{l2})$  denotes the event rate including the radiative decay, namely,  $N(\tilde{K}_{l2}) = N(K_{l2}) + N(K_{l2\gamma})$ , where  $N(K_{l2})$  and  $N(K_{l2\gamma})$  denote the rates of obtained events from  $K_{l2}$  and  $K_{l2\gamma}$  decays, respectively.  $K_{l2}$  events are identified by the toroidal spectrometer, and  $K_{l2\gamma}$  events are identified by the spectrometer and CsI(Tl) calorimeter with  $E_\gamma > 7$  MeV. This treatment of including the radiative decays is inevitable since their separation near the two-body decay peaks in the momentum spectra is difficult theoretically as well as experimentally with finite momentum resolution. The  $K_{l2}$  hadronic form factor can be canceled out by forming the ratio of the electric ( $K_{e2}$ ) and muonic ( $K_{\mu2}$ ) decay modes. Since both decay modes are measured simultaneously, the ambiguity of the number of stopped kaons does not contribute to the systematic uncertainty, and we do not need to take into account any effects from  $K^+$  intensity fluctuations during data accumulation. P36 aims for a sensitivity of  $\Delta R_K/R_K = \text{a few} \times 10^{-3}$  <sup>b)</sup>. This measured number of  $R_K$  is compared with the SM prediction under the assumption of  $\mu$ - $e$  universality, which is expressed, including the correction  $\delta_r$  ( $\sim 0.03$ ) due to the internal bremsstrahlung (IB), as

$$\begin{aligned} R_K^{SM} &= \frac{m_e^2}{m_\mu^2} \left( \frac{m_K^2 - m_e^2}{m_K^2 - m_\mu^2} \right)^2 (1 + \delta_r) \\ &= (2.477 \pm 0.001) \times 10^{-5}. \end{aligned} \quad (2)$$

The uncertainties in all the factors of Eq. (1) become sources of systematic uncertainties. They are categorized into a) uncertainties arising from the measurement, namely the ratio of  $N(\tilde{K}_{l2})$ , and b) uncertainties arising from the estimate of the acceptance ratio  $\Omega(\tilde{K}_{l2})$ . The uncertainty of  $N$  includes 1) the systematic uncertainties originating from the detector, 2) the systematic uncertainties due to backgrounds, and 3) the uncertainties arising from data analysis. The uncertainty of  $\Omega$  should also be estimated, yielding the total size of systematic uncertainty. In this report, all these sources of uncertainties are checked one by one in order as is shown in Table 2.

---

<sup>b)</sup> $\Delta R_K$  means the one-sigma error throughout this report.

Table 1: Summary of the main parameters of the lepton-universality-violation measurement in the P36 proposal.

Physics	Search for new physics in LU violation <sup>u)</sup>
Measured quantity	$R_K = \Gamma(\tilde{K}_{e2})/\Gamma(\tilde{K}_{\mu2})$
Sensitivity goal (statistical)	$\Delta R_K/R_K = 0.2\%$
Sensitivity goal (systematical)	$\Delta R_K/R_K \simeq 0.15\%$ <sup>v)</sup>
Sensitivity goal (total)	$\Delta R_K/R_K \cong 0.25\%$ <sup>v)</sup>
Beam	$K^+$ at K1.1BR
Beam momentum	750-800 MeV/ $c$
$K^+$ intensity	$2.2 \times 10^5/s$
$K^+/\pi^+$ ratio	$> 1$
Run time	60 days <sup>w)</sup>
$K_{e2}$ event selection	$p_e = 247$ MeV/ $c$ peak + rad. tail
$K_{\mu2}$ event selection	$p_\mu = 236$ MeV/ $c$ peak + rad. tail
$Br(K_{e2})^x)$	$(1.584 \pm 0.020) \times 10^{-5}$
$Br(K_{e2\gamma})^x)$	$(9.4 \pm 0.4) \times 10^{-6}$
$Br(K_{\mu2})^x)$	$(63.55 \pm 0.11) \times 10^{-2}$
$Br(K_{\mu2\gamma})^x)$	$(6.2 \pm 0.8) \times 10^{-3}$
$N(\tilde{K}_{e2})$	$250 \times 10^3$
$N(\tilde{K}_{\mu2})$	$\gg 10^6$ (depending on trigger)
Detector	Upgraded E246 detector
Momentum analysis	Superconducting Toroidal Magnet
Field strength	1.4 T
Radiative decay detection	CsI(Tl) calorimeter
PID ( $e^+/\mu^+$ )	AC $\otimes$ TOF $\otimes$ PGC
Tracking	3 MWPCs + 1 GEM + Fiber target
Trigger	$\check{C}(K^+) \otimes TOF2 \otimes AC$ ( + $SC \cdot [\check{C}(K^+) \otimes TOF2]$ )

We believe that the items discussed in this Addendum are covering all the conceivable sources of uncertainties before data are taken, and that their sizes have now been estimated. Of course, more exact analyses are possible based on the experimental data only after the data are taken. In any case the systematic error analysis will guide the construction of the new detector elements and will guide us when we perform the experiment.

Table 2: Categories of systematic errors according to Eq. (1)

Category	Source	Description
(A) Errors from measurement: $N(\tilde{K}_{e2})/N(\tilde{K}_{\mu2})$	1) Detector origin	Sec. 4
	2) Background origin	Sec. 5
	3) Analysis origin	Sec. 6
(B) Errors from acceptance estimate: $\Omega(\tilde{K}_{e2})/\Omega(\tilde{K}_{\mu2})$	Simulation etc.	Sec. 3, Sec. 7

### 3 Estimate of the $K_{e2}/K_{\mu2}$ acceptance ratio

#### 3.1 $K_{e2}/K_{\mu2}$ acceptance ratio as a direct source of a systematic error

One of the most essential points of this experiment is the estimate of the  $K_{e2}$  and  $K_{\mu2}$  acceptance of the detector, in particular their ratio  $Q = \Omega(\tilde{K}_{e2})/\Omega(\tilde{K}_{\mu2})$ . It is very relevant to the stopped  $K^+$  method of the proposed experiment, in which the acceptance is primarily determined by the finite solid angle of the detector system in contrast to the in-flight decay experiments where there is no such constraint but issues of difficult kinematical separation exist. Since  $R_K$  is deduced from the counting-rate ratio divided by  $Q$  (Eq. (1)), the uncertainty  $\Delta Q$  of  $Q$  affects directly  $R_K$ , namely,

$$\Delta R_K/R_K = \Delta Q/Q + \dots \quad (3)$$

and this can become the most serious source of the systematic uncertainty.

In the proposal and Addendum I, we only argued that we will perform a full Monte Carlo simulation based on a reliable code, and that the validity of the simulation can be checked against existing data of various observables (not necessarily the acceptance itself) from KEK-PS and possibly with P36 data. While we cannot avoid relying partially on Monte Carlo simulations, it is desirable to support the calculations of the acceptances using data. In this report we discuss the various possible methods to estimate the acceptance ratio  $Q$  using the existing data or future calibration data from P36. This gives us a more reliable estimate of the associated uncertainties.

---

<sup>u)</sup>Another physics goal of P36 is the search for heavy sterile neutrinos.

<sup>v)</sup>Updated value after this report.

<sup>w)</sup>The total run time of the ‘‘Lepton Universality’’ measurement part of P36, requested in the original proposal. It turned out in this report, that we need some additional time for systematic control and calibration runs, in order to minimize the systematic error. This is summarized in Section 8.

<sup>x)</sup>These numbers are from the Particle Data Book [16].

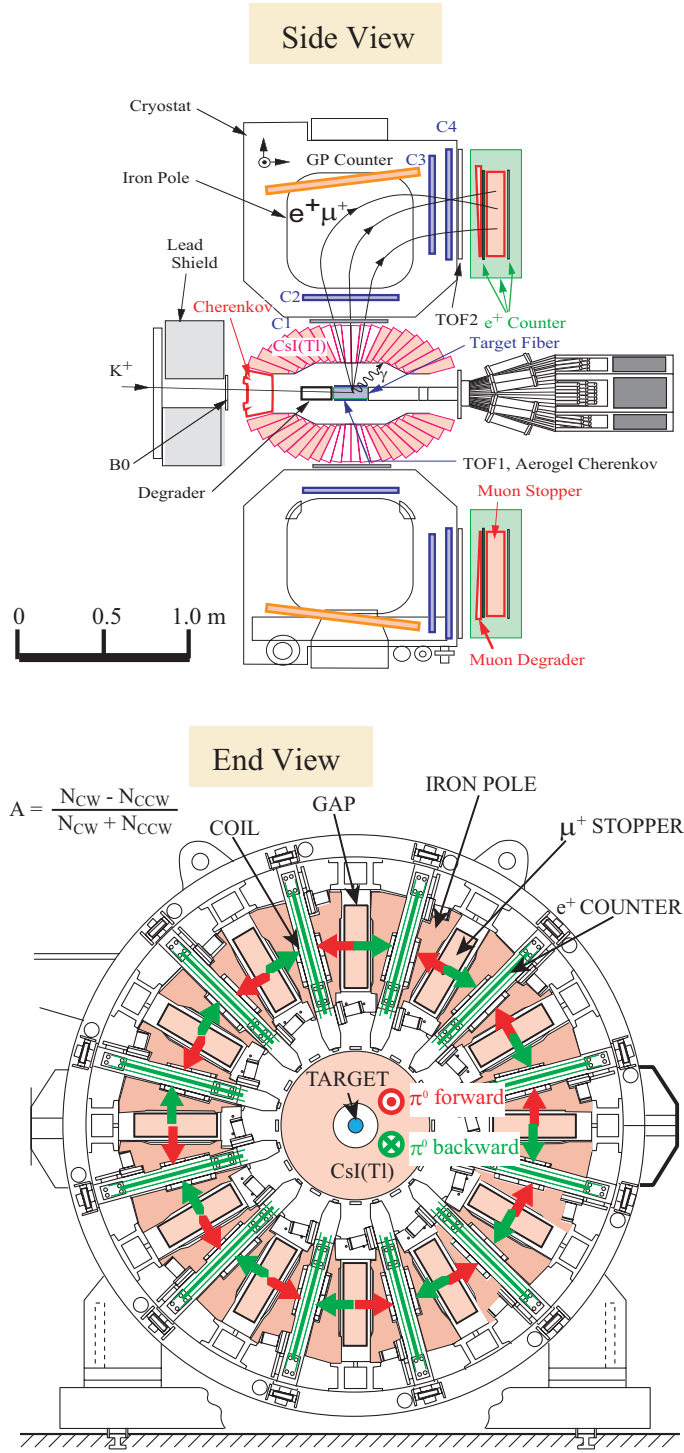


Figure 1: Cross sectional end- and side-views of the P36 setup for the  $R_K$  experiment. The E246 detector of KEK-PS is being upgraded. The momentum vectors of charged particles and photons are determined by the toroidal spectrometer and the CsI(Tl) calorimeter, respectively.

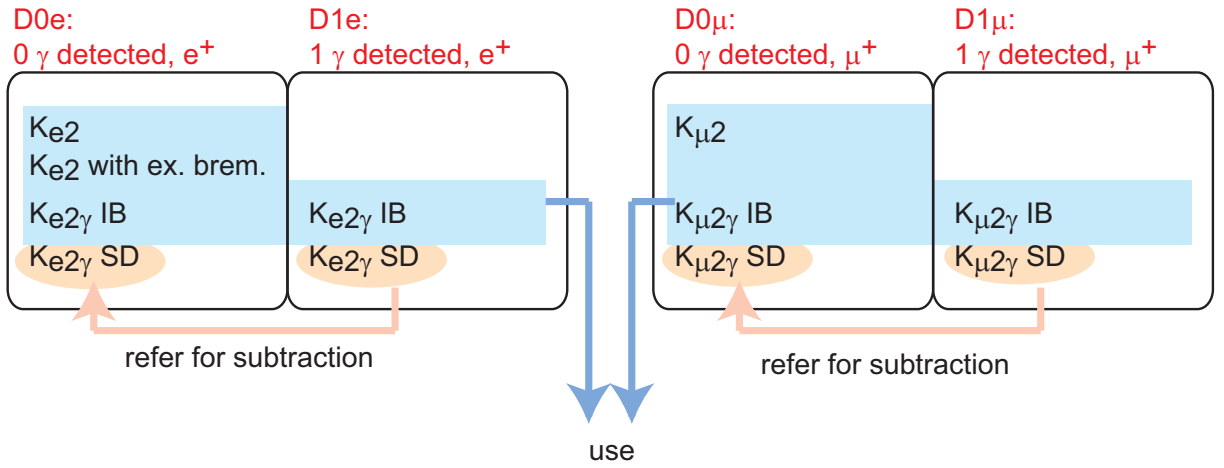


Figure 2: The schematic overview of data categories and data handling for each decay. Since the CsI(Tl) solid angle is not 100% the radiative decays are also detected without a hit of a photon in CsI(Tl). Each decay is grouped into D1 and D0, with a photon and without a photon detected, respectively. D1 events are identified by the CsI(Tl) hit with  $E_\gamma > \sim 7$  MeV. The radiative decays, internal bremsstrahlung (IB) and structure dependent (SD), are therefore present in all data groups. IB is inclusive in the analysis, however SD is a background and to be subtracted. Since we can understand the  $K_{l2\gamma}^{SD}$  kinematics carefully using the D1 data, we can correctly estimate this background fraction in D0 sample.

## 3.2 Factors contributing to the acceptance ratio

There are a few factors affecting the detector acceptance of the TREK setup for this stopped  $K^+$  experiment. In the experiment, the decay width is determined solely from the momentum spectra observed with the Toroidal spectrometer after discriminating the  $e^+$  and  $\mu^+$  with the particle ID scheme described in Section 4. The  $\tilde{K}_{e2}$  events are counted by integrating the momentum spectrum from 228 MeV/ $c$  over the 247 MeV/ $c$  peak, while the  $\tilde{K}_{\mu2}$  from 215 MeV/ $c$  over the 236 MeV/ $c$  peak, including the radiative decay tails<sup>c)</sup>. Thus, the acceptance difference for  $K_{e2}$  and  $K_{\mu2}$  detection comes from:

- Different decay momenta of 247 MeV/ $c$  and 236 MeV/ $c$  for  $K_{e2}$  and  $K_{\mu2}$ , respectively, which result in different solid angles for  $e^+$  and  $\mu^+$  in the spectrometer. The solid angle is limited by the magnet aperture, tracking chamber size, and trigger counter size etc., which have a different effect on various trajectory distributions depending on the particle momenta.
- Different interactions of the  $e^+$  and  $\mu^+$  in the  $K^+$  stopping target. These interactions produce momentum shifts due to ionization and radiation, angular ambiguity due to scattering, which affect the spectroscopy. Annihilation in the case of  $e^+$  is a direct loss of the acceptance.

These two factors have to be evaluated with a precision better than 0.1% in order to ensure the experimental accuracy of  $\Delta R_K/R_K \simeq 0.1\%$ . In the following we discuss these two points in detail. As long as these effects are small they can be treated additively.

## 3.3 Estimate of the spectrometer acceptance

With regards to the first point of different momenta, the estimate is not straightforward. We have to obtain a reasonable answer from a comparison between results of several methods. In the present case three methods are considered, as described next. They each have an advantage and a disadvantage. For exact discussions the radiative tails have to be taken into account. However, in the following subsections we will treat only the  $K_{l2}$  main peaks to simplify the discussion. This is justified as the relevant tails from IB are small, and the effects can be considered at the end, if necessary.

### 3.3.1 Pure Monte Carlo simulation

We can apply the Monte Carlo simulation code developed for the E246 experiment at the KEK-PS; the performance of the simulation code is well known to us. Start-

---

<sup>c)</sup>The tails due to IB are about 2% and 1% of the peak intensities, for  $\tilde{K}_{e2}$  and  $\tilde{K}_{\mu2}$ , respectively.

ing from a realistic  $K^+$  stopping distribution in the target<sup>d)</sup>, the decay  $e^+/\mu^+$  from  $K_{e2}/K_{\mu2}$  are tracked at a magnetic field of 1.4 T. The acceptance ratio,  $Q$ , is then determined from the accepted number of detected events,  $N_{MC}^{accept}(K_{l2})$ , and the total number of decays,  $N_{K_{l2}}^{decay}$ , as

$$Q = \frac{N_{MC}^{accept}(K_{e2} : B = 1.4 \text{ T})}{N_{K_{e2}}^{decay}} \bigg/ \frac{N_{MC}^{accept}(K_{\mu2} : B = 1.4 \text{ T})}{N_{K_{\mu2}}^{decay}}. \quad (4)$$

Here, very precise knowledge of the magnet geometry and detector configuration is required. The correctness of the simulation code can be checked by the reproducibility of various observables in several decay modes, such as  $K_{\mu3}$  or  $K_{e3}$  [5, 6, 7, 8, 9]. In Addendum I, we demonstrated e.g. that the spectra of an E246 special calibration run (with very limited statistics) could be fitted quite well with small  $\chi^2$ s.<sup>e)</sup> In Fig. 3, we show again the histograms of the momenta of  $e^+$  and  $\mu^+$  and their opening angles relative to the  $\pi^0$  momentum direction. Although the field strength in this case was 0.9 T, the following points can be confirmed:

- The two momentum spectra, Fig. 3 (b) and (d), including the relative height and the target energy-loss characteristics, could be fitted with the same acceptance function resulting in small normalized  $\chi^2/n = 0.94$  and  $1.07$  for  $K_{\mu3}$  and  $K_{e3}$ , respectively. (In the current case with relatively small statistics, the acceptance function does not take into account the interactions in the target such as bremsstrahlung, annihilation, and photon conversion.) The only free parameters in the fitting were the form factors and one intensity parameter.
- The form factors affect the opening angle spectra, Fig. 3 (a) and (c), significantly, but they produce only a very small effect on the momentum spectra. The spectrometer acceptance can be determined fairly uniquely in spite of the form factor ambiguity; the influence of the form factor ambiguity on  $Q$  will be discussed later in Subsections 3.3.3 – 3.3.4 in connection with the  $K_{\mu3}$  calibration method.
- The accuracy of the physics-parameter determinations was at the level of 1% in these fitting checks; this was sufficient for the previous experimental purpose. However we will need comparisons with an accuracy of 0.1% in this proposed experiment. The uncertainty of the form factors will no longer be negligible. Although we will accumulate 100 times more events and thus a comparison with higher accuracy becomes possible, the uncertainty of the form factors enters in the final uncertainty of the acceptance ratio<sup>f)</sup>. It is difficult to estimate it

---

<sup>d)</sup>The kaon stopping distribution in the target can be determined accurately in a simulation calculation which reproduces the  $\pi^+$  momentum spectrum and the  $\pi^+\pi^0$  opening-angle distribution of  $K_{\pi2}$  decays. The effect of the uncertainty in the stopping distribution on  $Q$  is discussed in Section 7.

<sup>e)</sup>Section 2 in Addendum I [2].

<sup>f)</sup>In order to achieve the best fit according to the variation of the form factors, we have to adjust the acceptance function.

reliably at the moment. However, it can be evaluated from the correspondence between the form factor uncertainty and the yields, to be roughly  $\Delta R_K/R_K \leq 0.06\%$ . It is not straightforward to extend the acceptance function to the higher momentum range of  $K_{e2}$  and  $K_{\mu2}$  and compare with data. Further investigations are required as shown in Section 3.3.3.

### 3.3.2 Estimate with the help of $K_{\mu2}$ peak

A second possible method to estimate the acceptance ratio,  $Q$ , is the use of experimental data from the  $K_{\mu2}$  decay with the monochromatic peak in the momentum spectrum in order to eliminate the uncertainty of the acceptance function. By reducing the field strength  $B = 1.4$  T for the real measurement to  $B = 1.34$  T with a reduction factor 0.955 ( $= 236 \text{ MeV}/c / 247 \text{ MeV}/c$ ), we can establish a  $K_{\mu2}$  trajectory distribution identical to the  $K_{e2}$  trajectory distribution up to a small effect due to field-distribution non-linearity. We will perform a special control run with this reduced field and count the number  $N(K_{\mu2}; B = 1.34 \text{ T})$  of  $K_{\mu2}$  events which should be normalized by the number of stopped  $K^+$ . The concept of this calibration is shown in Fig. 4. The ratio of the  $K_{e2}/K_{\mu2}$  acceptance  $Q$  is determined as,

$$Q = \frac{N(K_{\mu2}; B = 1.34 \text{ T})}{N(K_{\mu2}; B = 1.4 \text{ T})} \times \beta \times n, \quad (5)$$

where  $\beta$  is the correction factor for the magnetic field non-linearity due to pole-piece saturation, and  $n$  is the normalization factor of stopped  $K^+$ s, which are counted with the beam Cherenkov counter (see [1] for details and precision). Several remarks are as follows:

- The  $K_{\mu2}$ -peak event count should be obtained with an accuracy better than 0.1%. This determines the necessary run time for the control run; see Section 8 for the necessary run time. Also the peak analysis should be done with similar accuracy. This condition requires us to perform a measurement without any background in the momentum spectrum, as for  $K_{e2}$  peak in the real run.
- This method requires two separate control runs. The assumption is that the beam, target, and spectrometer remain stable in each of these runs and in the main data taking. Only under such condition this method can be applied. If the rate is sufficiently high, we can repeat these control runs regularly and thus mitigate any effects of slow variations of the experimental conditions.
- We do not have to consider the acceptance function of the CsI(Tl) photon detector in contrast to the method using  $K_{e3}$  and  $K_{\mu3}$  discussed next in which the photon detection is necessary to identify these decays clearly.

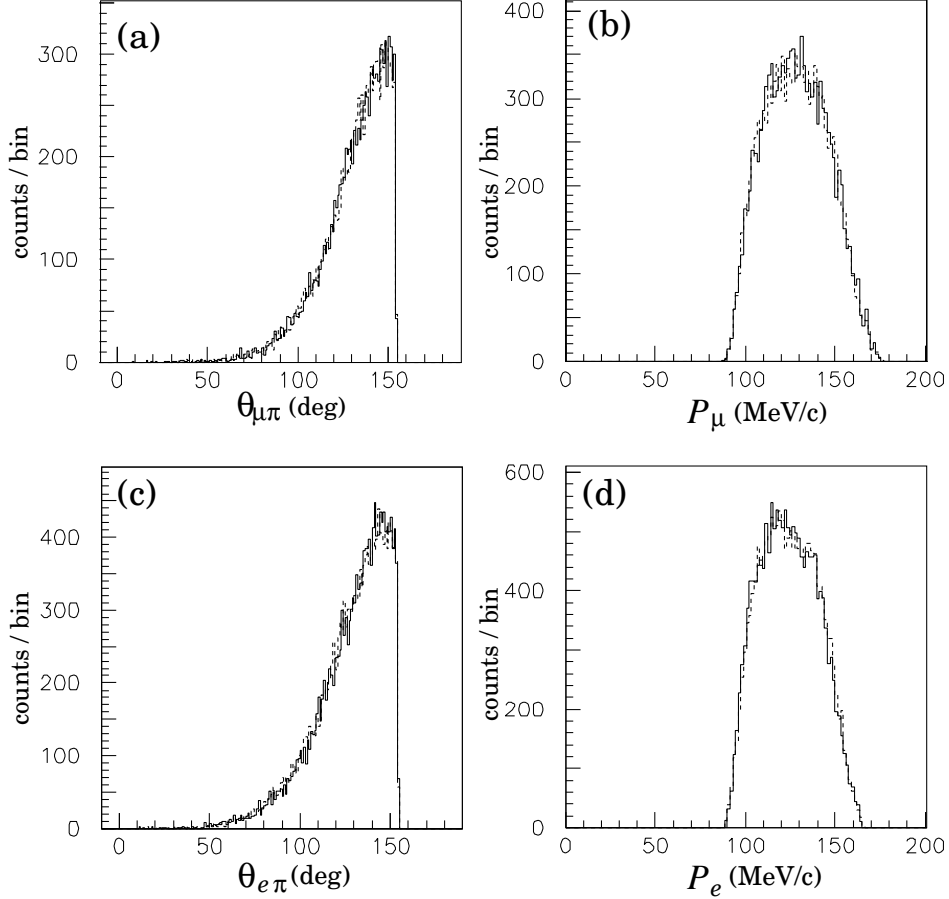


Figure 3: Demonstration of the validity of the Monte Carlo simulation calculation.  $K_{e3}$  and  $K_{\mu 3}$  spectra from an E246 special calibration run [6] at  $B = 0.9$  T. Panels (a) and (c) show the opening-angle distributions between the charged particle and the  $\pi^0$  momentum directions, panels (b) and (d) show the charged particle momenta without any energy loss correction in the target. Panels (a) and (b) are for  $K_{\mu 3}$ , and (c) and (d) are for  $K_{e3}$ . The solid and dotted lines are the experimental data and the best-fit Monte Carlo simulations using the same acceptance function, respectively. The only free parameters are the form factors, which could be reproduced consistent with the world average values. The fit form factors are  $\lambda_+ = (2.78 \pm 0.26 \pm 0.30) \times 10^{-2}$  for  $K_{e3}$  and  $\lambda_+ = (2.78 \pm 0.40) \times 10^{-2}$  and  $\lambda_0 = (1.90 \pm 0.64) \times 10^{-2}$  for  $K_{\mu 3}$  while the world average are,  $\lambda_+ = 0.0296 \pm 0.0017$  and  $\lambda_0 = 0.0196 \pm 0.0013$ , respectively. The initial  $K^+$  distribution in the target was tuned by using the two body decay of  $K_{\pi 2}$ . We see that the agreement is good, with  $\chi^2/n$  of (a) 1.12, (b) 0.94, (c) 1.10, and (d) 1.07. The  $K_{\mu 3}$  statistics is  $11 \times 10^3$  and  $K_{e3}$  is  $17 \times 10^3$ .

- The correction  $\beta$  is not large for the field difference between 1.4 T and 1.34 T. Although this effect is deduced in a simulation calculation, the partial use of the experimental  $K_{\mu 2}$  data should increase the reliability of this estimate. We will need a field mapping for  $B = 1.34$  T<sup>g)</sup>.

Since we can accumulate  $K_{\mu 2}$  events with a high rate, the uncertainty will be dominated by the uncertainty of  $\beta$ , which is not known at the moment. Nevertheless we can give the following qualitative discussion. We have performed a simulation calculation under the simplest condition of a point source without any material. The spectrometer acceptance factor  $\beta$  is then related to the field distribution through the quantity  $\langle \int B \cdot dl \rangle$ , where the average is taken over trajectories, and can be determined in a 3D magnetic field calculation TOSCA with an accuracy of better than  $10^{-3}$ , since the mapping precision is usually  $10^{-3}$ .  $\beta$  is just the ratio of this quantity for two different momenta under the corresponding field strength. Since any field errors must be common to both trajectories, the ratio reduces this uncertainty. We assume a cancellation factor of 100, resulting in the uncertainty of  $\sim 10^{-5}$  in the case of 1.34 T v.s. 1.4 T. In the case of 0.9 T v.s. 1.4 T which is used in the  $K_{\mu 3}$  calibration discussed later, the cancellation factor may not be as large; however, we can expect a factor of at least 10, giving a  $\beta$  uncertainty of  $10^{-4}$ .

### 3.3.3 Estimate with the help of $K_{\mu 3}$ spectrum

In order to avoid the uncertainty of the beam-intensity normalization  $n$  involved in the estimate using the  $K_{\mu 2}$  peak, we can use the broad momentum spectrum of  $K_{\mu 3}$  (and  $K_{e 3}$ ) as indicated earlier. By reducing the field strength down to 0.9 T we can overlap the  $K_{\mu 3}$  spectrum with the  $K_{e 2}$  and  $K_{\mu 2}$  momentum region at  $B = 1.4$  T. We will perform a special control run at this field strength. The acceptance ratio for particle momenta of 164 MeV/ $c$  and 157 MeV/ $c$  from the  $K_{\mu 3}$  decay corresponds to the acceptance ratio of  $K_{e 2}$  and  $K_{\mu 2}$  at  $B = 1.4$  T up to the field non-linearity correction. This method is illustrated in Fig. 5. The ratio  $Q$  is written as,

$$Q = \frac{N(K_{\mu 3}; B = 0.9 \text{ T}; 164 \text{ MeV}/c)}{N(K_{\mu 3}; B = 0.9 \text{ T}; 157 \text{ MeV}/c)} \times \alpha \times \beta' \times \gamma. \quad (6)$$

As mentioned before we have to identify  $K_{\mu 3}$  events by also detecting  $\pi^0$  mesons, the ratio  $N(164 \text{ MeV}/c)$  and  $N(157 \text{ MeV}/c)$  has to be corrected for the CsI(Tl) acceptance ratio  $\gamma$  (which depends on the  $\pi^0$  energy and thus on the muon momentum) in addition to the spectral-shape correction  $\alpha$  determined by the form factors. The field calculation at 0.9 T is now under way. The field effect correction  $\beta'$  will be evaluated in a simulation calculation. A few more remarks are as follows:

- We do not need to normalize by the beam intensity, or run time. Thus, this method is free from beam instability and other time-dependent detector conditions during the control run. Of course significant change of the kaon stopping

<sup>g)</sup>The 3D field calculation at  $B = 1.34$  T is under way. The correction factor  $\beta$  and its uncertainty will be extracted.

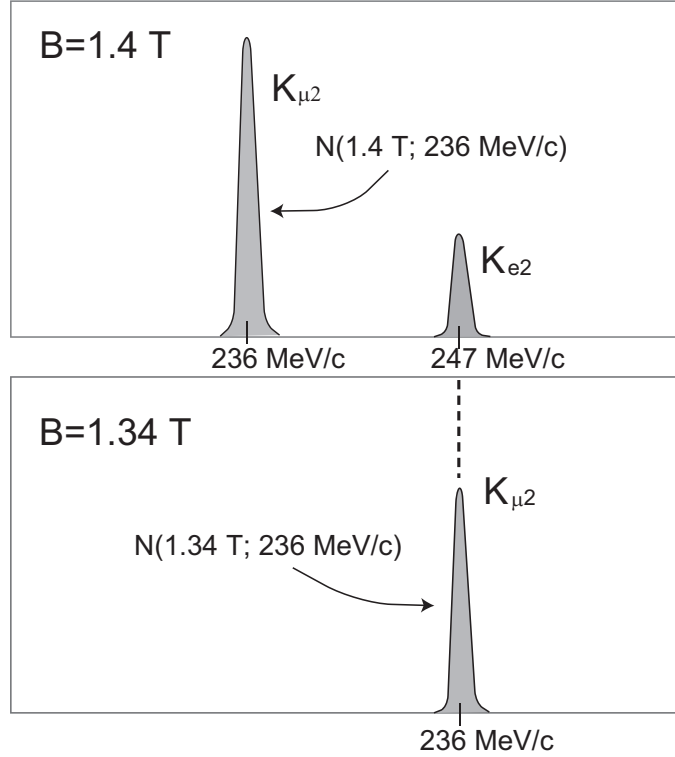


Figure 4: The acceptance-ratio calibration by using  $K_{\mu 2}$  is shown schematically. By reducing the field strength from  $B = 1.4$  T to  $B = 1.34$  T in a calibration run, we can realize a similar trajectory distribution for  $K_{\mu 2}$  events as for  $K_{e 2}$  at 1.4 T in the main experiment. The ratio of  $K_{\mu 2}$  in the two measurements provides the acceptance ratio of particles with momenta of 247 MeV/ $c$  and 236 MeV/ $c$  up to a small correction due to the effect of field non-linearity. The uncertainty comes mainly from this field-effect correction and beam normalization, if the spectra are free from backgrounds. If the energy loss in the target is significant, the effect will have to be included.

distribution in the target limits the applicability of this method, unless we repeat the control runs frequently. Realistic run times are summarized in Section 8.

- Although we need a simulation calculation at  $B = 0.9$  T, and the correction by the spectral shape and CsI(Tl) efficiency, we regard that the partial use of the experimental data strengthens the reliability of this estimate.
- The calibration run will be performed using a thin target. If we have to use a thick target, the energy loss in the target should be taken into account by lowering the field strength further. The energy-loss correction brings about an additional uncertainty.

In the next subsection we discuss the detailed analysis procedure by using the old E246 data and an estimate of the error.

### 3.3.4 Estimate by the E246 $K_{\mu 3}$ data

We will now estimate  $Q$  with the help of the  $K_{\mu 3}$  peak described in the previous subsection by using the E246 data and we will extract the error in the acceptance ratio. It is possible to extract the spectrometer acceptance curve from the data. Fig. 6(a) shows the Monte Carlo-generated Dalitz density plot applying the muon energy loss in the target. The absolute number of generated events can be somewhat arbitrary since we take a ratio at the end. The PDG world average of the  $K_{\mu 3}$  form factors was used to generate events Fig. 6(b) is the acquired E246  $K_{\mu 3}$  data. The Dalitz acceptance plot  $A(p_{\mu}, p_{\pi^0})$  (Fig. 6(c)) is obtained by dividing the experimental data of Fig. 6(b) by the simulation of Fig. 6(a). Next the CsI(Tl) response  $\epsilon(p_{\mu})$  was calculated in a Monte Carlo simulation as a function of the muon momentum, since the  $p_{\pi^0}$  distribution is dependent on  $p_{\mu}$ . Fig. 6(d) show the result. Although there is some gradient is seen (depending on the form factors), the response is quite flat. By dividing the projection of  $A(p_{\mu}, p_{\pi^0})$  (Fig. 6(e)) by the CsI(Tl) response function  $\epsilon(p_{\mu})$  we obtain the spectrometer acceptance function  $\Omega_{sp}(p_{\mu})$  as in Fig. 6(f). The acceptance ratio is then determined to be  $Q = \Omega(164 \text{ MeV}/c)/\Omega(157 \text{ MeV}/c) = 1.038 \pm 0.016$ . Here, the error of  $\pm 0.016$  is a statistical one from the experiment as well as MC simulation, which can be improved by a factor more than 10 with the higher statistics at P36. <sup>h)</sup>

The systematic errors in this analysis come from 1) the ambiguity of the form factors in the MC event generation, 2) the uncertainty of the energy loss in the target, 3) the uncertainty of the CsI(Tl) response function from the MC calculation, and 4) the reading error of the curve (f) at 164 MeV/ $c$  and 157 MeV/ $c$ . Among them it was found that 3) is dominant and much larger than 1) with the same reason of the form factor ambiguity. By taking the currently-known form factor ambiguity [16] of  $\lambda_+ = 0.0296 \pm 0.0017$ ,  $\lambda_0 = 0.0196 \pm 0.0013$ , the error from 3) is calculated to be

---

<sup>h)</sup>The best reading of the acceptance function was achieved by fitting the relevant region of (f) with a superposition of several polynomials.

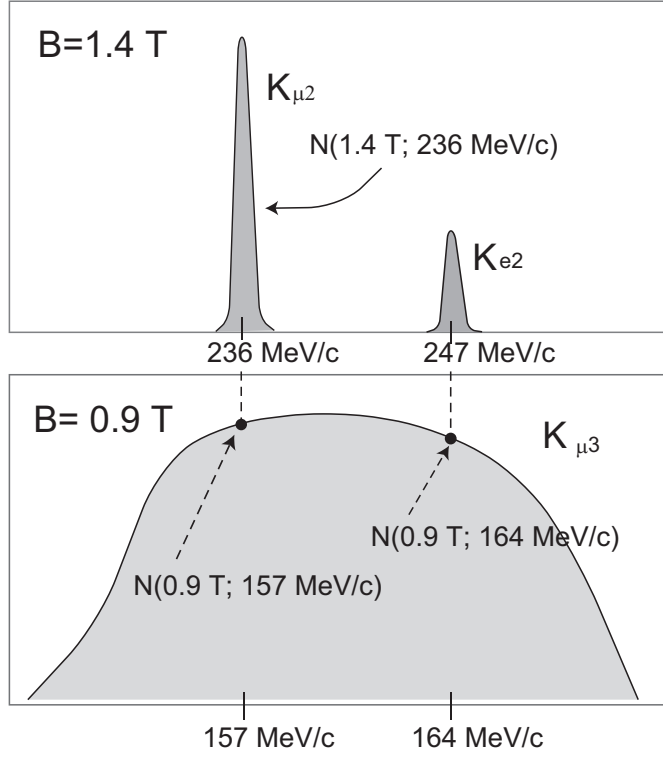


Figure 5: The acceptance-ratio calibration by using  $K_{\mu 3}$  is shown schematically. By reducing the field strength from  $B = 1.4$  T to  $B = 0.9$  T in a calibration run, we can realize coverage of similar trajectories for  $K_{\mu 2}$  and  $K_{e 2}$  events at 1.4 T of the main experiment. The ratio of  $K_{\mu 3}$  at 164 MeV/c and 157 MeV/c divided by the  $K_{\mu 3}$  spectral ratio  $\alpha$  provides the acceptance ratio of 247 MeV/c and 236 MeV/c up to a correction due to the effect of field non-linearity. CsI(Tl) acceptance is also corrected with the  $\gamma$  factor. A normalization of the beam intensity is not necessary in this method. This figure is based on the assumption of no energy loss in the target. If we use a thick target in the calibration run and the energy loss is not negligible, the effect has to be corrected.

$\Delta Q/Q = 0.06\%$  <sup>i)</sup> before the field correction  $\beta$ . The error from 2) is calculated to be  $\Delta Q/Q = 0.05\%$  assuming the energy loss uncertainty corresponding to the material thickness uncertainty of 0.5 mm in the target. It was confirmed that the error from 4) will be small by using a polynomial fit scaling to a statistical fluctuation of the total events. Regarding the field correction, we have to wait for the results of 3D field mapping and tracking studies before extracting an error. However, we expect that the error from the form factor ambiguity should be larger. Thus, we may conclude that the total size of the systematic error from these effects can be obtained by adding the systematic sources of 2) and 3) to be

$$\Delta R_K/R_K = 0.00078. \quad (7)$$

### 3.4 $e^+/\mu^+$ interactions in the target

The effects of  $e^+/\mu^+$  interaction in the target affecting  $Q$  can be categorized in two groups:

1. Disappearance of the  $e^+$  due to annihilation in flight and external bremsstrahlung with a photon of relatively high energy.
2. Emission angle ambiguity from the target and momentum shift due to the target energy loss and multiple scattering, which bring some uncertainty in estimating the spectrometer acceptance discussed before.

Regarding the first point, its estimate relies on the simulation calculations. Since we set a threshold on the  $e^+$  momentum spectrum just above the  $K_{e3}$  edge, the events with a high energy photon are rejected. The largest error is considered to come from the uncertainty of the bremsstrahlung estimate; this will be discussed in detail in Section 7.3.3.

We are also relying primarily on a MC simulation for the second point. The effects can be implemented in the MC simulation to estimate the spectrometer acceptance, as was shown before in Section 3.3.3. However, we want to strengthen the validity of the estimates by using data. We can compare the  $K_{e3}$  and  $K_{\mu3}$  events at the same momentum. After correcting for the branching ratio and the spectral shape determined by the form factors in both decays, the event number ratio should reflect the effects from the scattering and the momentum shift. The scan of this analysis over the  $K_{\mu3}/K_{e3}$  momentum region provides us some estimate of the effects, which can be extrapolated to the higher momentum region of  $K_{\mu2}$  and  $K_{e2}$ . The error associated with this effect can be regarded to be smaller than that from the first point.

---

<sup>i)</sup>This error involves both of the MC simulation statistical error and the error from the form factor uncertainty. At this moment, we regard this number is due to the form factor uncertainty for a safe side estimate

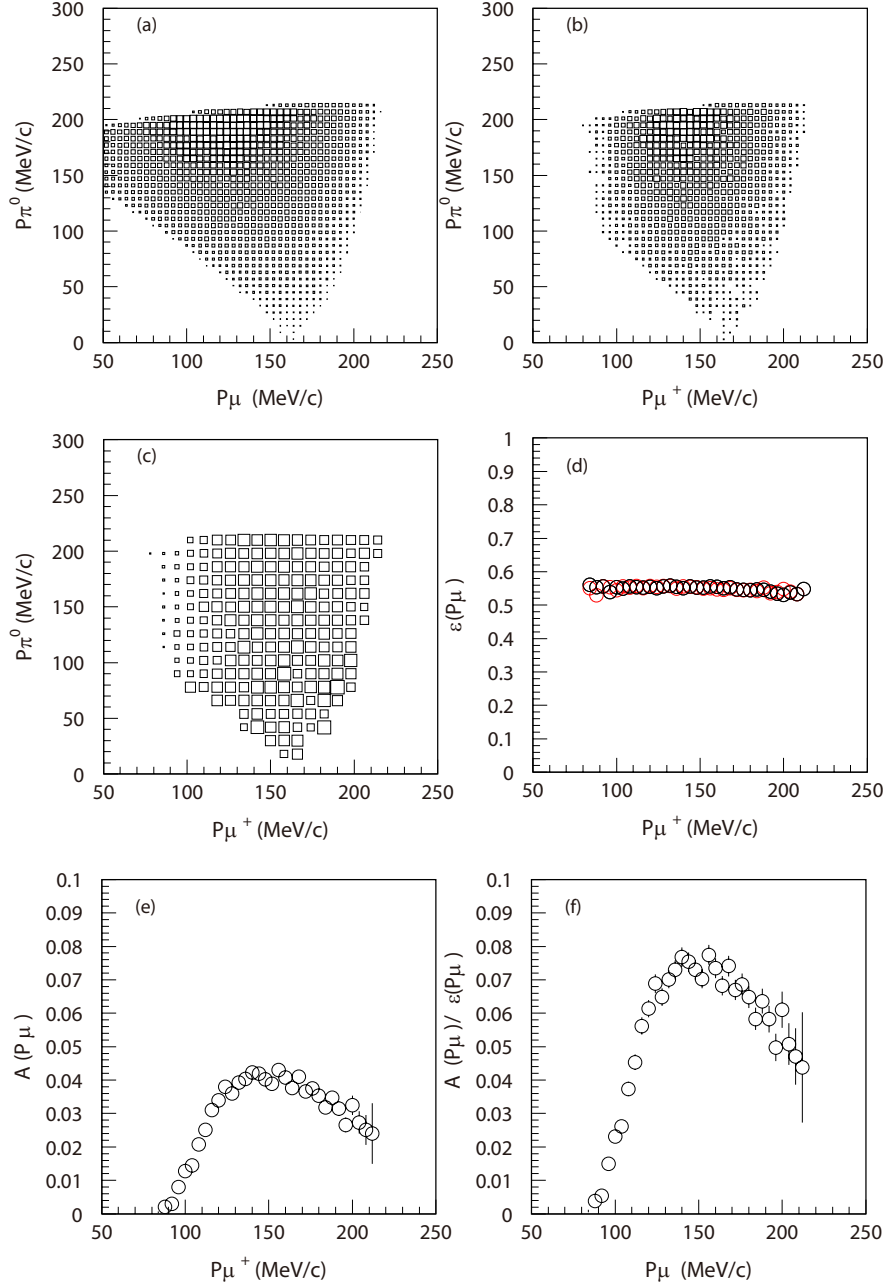


Figure 6: Estimation of the acceptance ratio with the E246  $K_{\mu 3}$  data. (a) the MC-generated Dalitz density plot at birth but after the energy loss in the target by using the  $K_{\mu 3}$  form factors of PDG world average. (b) the Dalitz density plot of the acquired E246  $K_{\mu 3}$  data. (c) The Dalitz acceptance plot  $A(p_{\mu}, p_{\pi^0})$  is obtained by dividing (b) by (a), (d) CsI(Tl) response function  $\epsilon(p_{\mu})$ : the black plot is the function from the PDG form factors while the red maximum deviation within the  $2\sigma$  variation of form factors. The Q deviation is less than 0.06%. (e) projection of  $A(p_{\mu}, p_{\pi^0})$  onto  $p_{\mu}$ , and (f) the final acceptance function of the spectrometer.

## 4 Systematic errors from the measurement (1) – Detector performance–

### 4.1 Errors due to chamber inefficiency

Although all the tracking chambers of C1, C2, C3 and C4 are made with the technically-possible highest efficiency, we also have to anticipate a small but non-zero inefficiency in each chamber. Primarily the inefficiency is corrected for by using data as was explained in Addendum 1. The uncertainty of the correction, in particular the eventual difference between the positrons and the muons introduces a systematic error. In this report, we repeat the correction method again in more detail and re-evaluate the resulting error for  $R_K$ .

#### 4.1.1 Tracking efficiency

As was expressed symbolically with Eq. (7) in the previous Addendum 1, the tracking efficiency  $\epsilon_t$  for each trajectory is described as;

$$\epsilon_t = \epsilon_1(x1, y1) \times \epsilon_2(x2, y2) \times \epsilon_3(x3, y3) \times \epsilon_4(x4, y4) \times \epsilon_c. \quad (8)$$

Here,  $\epsilon_i(xi, yi)$  are the efficiencies of the  $i$ -th chamber at the position  $(xi, yi)$ . In general, MWPCs can have incident angle dependence in the efficiency, however, we deal here only with the position dependence which can be due to the anode wire characteristics and the cathode readout threshold. Furthermore they can be different because the positrons and muons have slightly different ionization characteristics.  $\epsilon_c$  is the event remaining probability after the trajectory fitting and the  $\chi^2$  cut. Events suffering large multiple scattering through the chambers are usually rejected in the physics analysis by this  $\chi^2$  cut. This can also be particle dependent. In order to achieve a high accuracy in  $R_K$  we need to have an exact knowledge of  $\epsilon_t$  for  $e^+$  and  $\mu^+$  individually.

#### 4.1.2 Efficiency measurement

We will employ  $K_{e2}$  and  $K_{\mu2}$  events themselves and possibly  $K_{e3}$  and  $K_{\mu3}$  events for the efficiency calibration. Only for the chamber efficiency problem we may loosen the  $\chi^2$  cut and assume  $\epsilon_c$  to be almost 1.0 for the current discussion. A more exact comparison of  $\epsilon_c$  between  $e^+$  and  $\mu^+$  is given later (Section 4.1.5). For the  $K_{e2}$  the full data set of the main run will be used. For  $K_{e3}$  and  $K_{\mu3}$  events will be accumulated in a special calibration run at a reduced field strength of 0.9 T in relatively short time and the run will be repeated regularly if necessary. Trajectories which fall into the chamber spatial acceptance will be selected. Then the efficiency of the interested chamber, e.g. C3 can be calculated in the ratio of four-fold to three-fold coincidence with its position dependence for each trajectory as

$$\epsilon_3(x_3, y_3) = \frac{n(C1 \otimes C2 \otimes C3 \otimes C4)}{n(C1 \otimes C2 \otimes C4)}, \quad (9)$$

for  $e^+$  and  $\mu^+$ , respectively. with the particle ID with TOF and AC. Here  $C_i$  are the hit condition of the  $i$ -th chamber. Table 5 shows the summary of the measurements.

#### 4.1.3 Tracking efficiency of $K_{e2}$ and $K_{\mu2}$

Next we will consider how to extract the tracking efficiency and correct for it in the main measurement. Since the chamber efficiency may be dependent on each anode wire and the readout cathode threshold setting, it is desirable to calculate the tracking efficiency by using the position dependent chamber efficiencies for each trajectory using the relation Eq. (8). However, we will need a large amount of calibration data of  $\epsilon_i(x_i, y_i)$  with high statistics for all the segmentations. In the following we will discuss first an approximate method in terms of average chamber efficiency  $\bar{\epsilon}_i$ , which are valid when the position dependent inefficiencies are sufficiently small. After that we will discuss the exact method at the third bullet below. There are two conceivable methods to extract the average chamber efficiency of  $K_{e2}$  and  $K_{\mu2}$  as shown in the first two bullets below.

- **Method 1:** We can employ the actual experimental data of  $K_{e2}$  and  $K_{\mu2}$ . Since the trajectory distribution is exact, we can deduce a reliable result. The chamber average efficiency  $\bar{\epsilon}_i$  is then extracted as (e.g. for C3)

$$\bar{\epsilon}_3 = \frac{N(C1 \otimes C2 \otimes C3 \otimes C4)}{N(C1 \otimes C2 \otimes C4)}. \quad (10)$$

The  $K_{e2}$  and  $K_{\mu2}$  real event rates are then extracted as  $N(K_{\mu2}) \propto (\bar{\epsilon}_1 \cdot \bar{\epsilon}_2 \cdot \bar{\epsilon}_3 \cdot \bar{\epsilon}_4)_\mu^{-1}$  and  $N(K_{e2}) \propto (\bar{\epsilon}_1 \cdot \bar{\epsilon}_2 \cdot \bar{\epsilon}_3 \cdot \bar{\epsilon}_4)_e^{-1}$ . This analysis can be performed only after taking the main data. This method is a good approximation only when the inefficiency of each chamber is sufficiently small.<sup>j)</sup>

- **Method 2:** One selects 164 MeV/ $c$  events and 157 MeV/ $c$  events for  $K_{e3}$  and  $K_{\mu3}$  respectively, at the reduced field strength of 0.9 T, in order to simulate the  $K_{e2}$  and  $K_{\mu2}$  trajectory distribution at 1.4 T, and measures the average  $\bar{\epsilon}_t$ . This should nearly reproduce the tracking efficiencies of  $K_{e2}$  and  $K_{\mu2}$ , since the chamber hit-positions are almost the same. In an exact observation, there is a small difference in the trajectory distribution due the non-identical field shape between 1.4 T and 0.9 T due to magnet saturation. However, the difference

---

<sup>j)</sup>If we look at the chamber  $C_i$  the product of its inefficiency  $\delta\bar{\epsilon}_i$  and the sum of inefficiencies of other chambers  $\Delta\bar{\epsilon} = \sum_{j=1}^3 \delta\bar{\epsilon}_j$  should be small enough, namely  $\delta\bar{\epsilon}_I \cdot \Delta\bar{\epsilon} \ll 10^{-3}$ . This means that every chamber should have the inefficiency of  $\delta\bar{\epsilon}_I \ll 3 \times 10^{-2}$ . In the real cases where the large distribution of the trajectory angle randomizes the inefficiency distribution of the sandwiching trigger chambers, this condition should be much looser.

between the  $e^+$  and  $\mu^+$  is very small for the close momenta of  $K_{e2}$  and  $K_{\mu2}$ . The same analysis procedure as in the first bullet is performed, and the applicability argument is also the same.

- **Method 3:** If the efficiency has a strong position dependence in C1, C2 and C4, Eq. (9) is no longer valid. We will then have to carry out a more exact analysis taking into account the position dependence of each chamber. For the moment we assume about 100 segmentations either in  $x$  or in  $y$  direction depending on which has a stronger dependence. For each trajectory part the tracking efficiency can be calculated and then averaged to deduce the overall tracking efficiency. One uses  $K_{e3}$  and  $K_{\mu3}$  at reduced magnet field of 0.9 T. This calibration run will be repeated as the Method 1 or 2 during the main data taking if necessary.

#### 4.1.4 Error estimate

In the first method we can use all the experimental data. The error will be dominated by the  $K_{e2}$  number of events. The anticipated total number will be  $250 \times 10^3$  in the 12 spectrometer gaps. Now we may regard  $\bar{\epsilon}_i$  as the average value over the 12 gap chambers without losing the approximation validity. Assuming that we can fully use these events for all the chambers of C1, C2, C3 and C4, the determination accuracy of  $2.0 \times 10^{-4}$  for  $\bar{\epsilon}_i$  is obtained for e.g.  $\bar{\epsilon} = 0.99^k$  for each plane. The uncertainty of the total tracking efficiency in the worst case will be then  $4.0 \times 10^{-4}$  resulting in the same number for  $\Delta R_K/R_K^l$ .

In the second method we may assume that we take the momentum bite of 10% at the desired momenta. Then we expect about  $3.3 \times 10^5$  and  $2.5 \times 10^5$  events for  $K_{e3}$  and  $K_{\mu3}$  respectively in a special calibration run of 3 days at 30 kW beam power. If we apply the same argument as above and assume  $\bar{\epsilon}$  to be 0.99, we can achieve an accuracy of  $3.4 \times 10^{-4}$  and  $4.6 \times 10^{-4}$ , respectively, in the total tracking efficiency. The error in the difference, which contributes to  $\Delta R_K/R_K$ , will thus be  $6 \times 10^{-4}$ .

In the third method we use the  $K_{e3}$  and  $K_{\mu3}$  with the whole momentum spectra. In a 5 day calibration run we can accumulate  $5.5 \times 10^6$  events and  $3.3 \times 10^6$  events for both modes, respectively. By applying the same arguments as above also assuming  $\epsilon = 0.995$  we expect an accuracy of  $3.0 \times 10^{-4}$  and  $3.9 \times 10^{-4}$ , respectively, for each segment. The contribution from 4 chamber tracking is larger than 2 times.

Hence the  $e^+/\mu^+$  difference relevant to  $R_K$  leads to  $\Delta R_K/R_K = 10.3 \times 10^{-4}$  after averaging over the trajectory distributions.

Although the above arguments are semi-quantitative to some extent, these are the best estimates we can make before taking data. The error estimates are summarized in Table 3 also for the inefficiency cases of 0.5%, 1.0%, and 2.0%<sup>m</sup>.

<sup>k</sup>)The typically achieved chamber efficiency for C2, C3 and C4 in E246.

<sup>l</sup>)Here, the error of chamber efficiency was calculated with  $\delta\bar{\epsilon} = \sqrt{\bar{\epsilon}(1-\bar{\epsilon})}/\sqrt{N}$  resulting in the same number in  $\Delta R_K/R_K$ .

<sup>m</sup>)It is unpractical to apply Method 3 when the average chamber efficiency is low. We put the case

Table 3: Estimate of systematic error due to chamber inefficiency given for three possible methods of efficiency calibration. The error is dependent on the degree of efficiency.

Method	Mode@field	Time	$\epsilon$ or $\bar{\epsilon}$	$\Delta R_K/R_K$
1 average $\bar{\epsilon}$	$K_{e2}/K_{\mu2}$ @ 1.4 T	total run	0.98	$5.6 \times 10^{-3}$
			0.99	$4.0 \times 10^{-4}$
			0.995	$2.8 \times 10^{-4}$
2 average $\bar{\epsilon}$	$K_{e3}/K_{\mu3}$ @ 0.9 T	3 days	0.98	$8.0 \times 10^{-4}$
			0.99	$5.7 \times 10^{-4}$
			0.995	$4.1 \times 10^{-4}$
3 $\bar{\epsilon}(x, y)$	$K_{e3}/K_{\mu3}$ @ 0.9 T	5 days	0.995	$10 \times 10^{-4}$

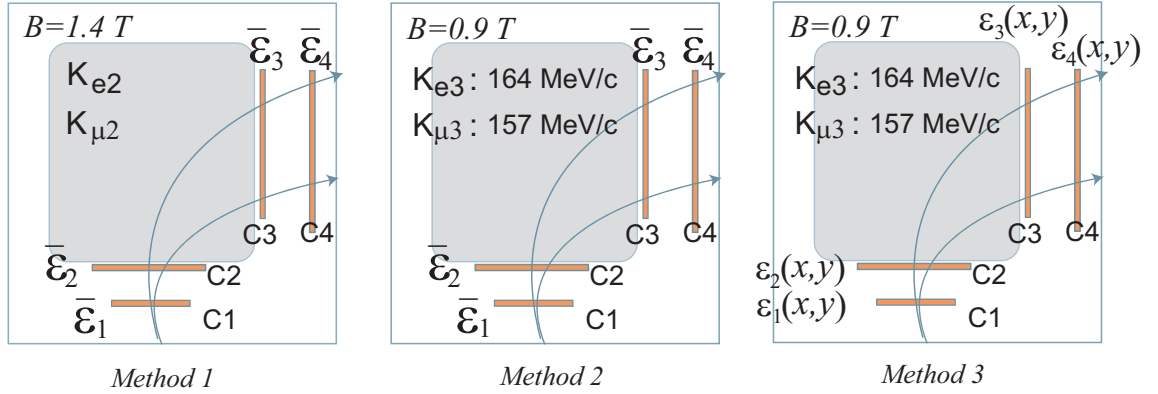


Figure 7: Three possible methods of chamber efficiency calibration. Method 1 is the use of the real data of  $K_{e2}$  and  $K_{\mu2}$  in the main measurement. Method 2 is the use of  $K_{e3}$  and  $K_{\mu3}$  decays at specific momenta at a reduced magnetic field of 0.9 T simulating similar trajectory distributions as  $K_{e2}$  and  $K_{\mu2}$ . In these calibrations only the average efficiency of each chamber is obtained. Method 3 is the efficiency measurement taking into account the position dependence in each chamber.

Table 4: Thickness (in radiation length  $X_0$ ) and average flight length to C4 from each tracking element

Chamber	Thickness ( $X_0$ )	Afterlength (m) <sup>t)</sup>
C1 (GEM)	0.0070	$\sim 1.5$
C2 (MWPC)	0.0027	$\sim 1.2$
C3 (MWPC)	0.0027	$\sim 0.3$
C4 (MWPC)	0.0027	-

Table 5: Summary of the performance check for the tracking elements. The efficiency can be determined by comparing signals from a particular element with the tracks reconstructed by the others.

Element checked	Tracking elements	PID
C1	C2, C3, C4	TOF $\otimes$ AC $\otimes$ PGC
C2	C1, C3, C4	TOF $\otimes$ AC $\otimes$ PGC
C3	C1, C2, C4	TOF $\otimes$ AC $\otimes$ PGC
C4	C1, C2, C3	TOF $\otimes$ AC $\otimes$ PGC

#### 4.1.5 Multiple scattering

The different characteristics of multiple scattering between the  $e^+$  and the  $\mu^+$  produces tracking efficiency difference through  $\epsilon_c$  in Eq. (8). We have to reject events with large  $\chi^2$  values in order to make the data samples free from backgrounds. The main Gaussian part of the Molière distribution is wider for muons at the same momentum, but the effects from atomic electrons might be different for a muon beam and positron beam. Of course the cut condition should be loosened as much as possible in the current experiment in order to avoid a systematic bias.  $\chi^2$  is formed as the sum of fit trajectory displacement-squared. In Table 4 we list the thickness of the four chambers and thereafter flight length in the average.

Fig. 8 is the simulated  $\chi^2$  distribution for  $K_{e2}$  and  $K_{\mu2}$ . The differences of  $\epsilon_c$  between  $e^+$  and  $\mu^+$  are obtained to be 0.0037 and 0.0015 for the cut at 20 and 30, respectively. The most troubling background, muon decay-in-flight ( $\mu$ -DIF), can be treated as a muon as long as the decay takes place after the AC. There is no worry about the  $K_{\mu2}$  event admixture into  $K_{e2}$ , even if a very loose  $\chi^2$  cut fails to detect a kink of  $\mu$ -DIF. Thus, we may open the  $\chi^2$  cut practically fully with no contribution to  $\Delta R_K/R_K$ .

---

of 0.5% inefficiency.

<sup>t)</sup>Average distance to C4.

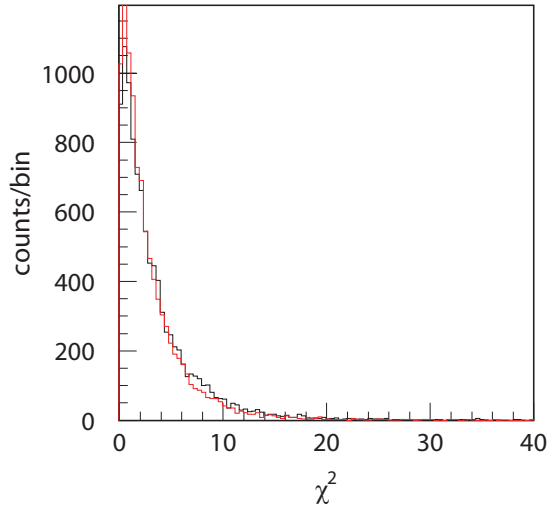


Figure 8:  $\chi^2$  distribution calculated in a Monte Carlo simulation with four chambers of C1, C2, C3, and C4 for  $K_{\mu 2}$  (black) and  $K_{e 2}$  (red). The  $\chi^2$  is caused by multiple scattering in these chambers. Although a slight difference between  $\mu$  and  $e^+$  can be seen, we may open the cut fully with a consequence of no difference in  $\epsilon_c$ .

## 4.2 PID performance

### 4.2.1 Anticipated performance of AC and TOF

Particle identification between the  $e^+$  and  $\mu^+$  will be carried out by measuring the time-of-flight between the TOF1 and TOF2 counters and by using the AC counter. TOF1 and TOF2 are located surrounding the  $K^+$  target system and 1 m behind the C4 chamber, respectively. The AC is installed between the TOF1 and the CsI(Tl) barrel. Properties to indicate the detector performance are shown in Table 6. Fig. 9 shows the expected mass squared spectrum ( $M_{\text{TOF}}^2$ ) calculated under the assumption of the timing resolution of  $\sigma_t = 100$  ps. The  $e^+$  efficiency and  $\mu^+$  mis-identification probability are obtained to be 99.9% and 0.1%, respectively. The performance of the AC counter was studied by constructing a prototype counter and testing it at the Research Center for Electron Photon Science, Tohoku University. Using the results of the test experiment, further improvements to the new AC counter design have been made, and the  $e^+$  efficiency is now estimated to be 99.88%.

### 4.2.2 Addition of a Pb-glass counter for PID

As already explained in Addendum 1, we intend to add a Pb-glass Cherenkov detector (PGC) with 10 cm in thickness to each gap. The PGC will be placed just behind TOF2, as shown in Fig. 10 of the PID system. This detector plays a supplementary role in the particle identification for the TOF and AC efficiency determinations. The properties of the PGC system are summarized in Table 7. Here we see sufficiently

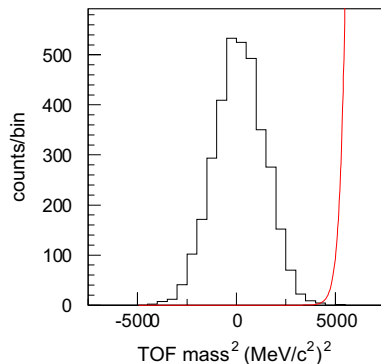


Figure 9: The expected mass squared spectrum ( $M_{\text{TOF}}^2$ ) from the TOF measurement calculated under the assumption of the timing resolution of  $\sigma_t = 100$  ps.

Table 6: Properties of the TOF and AC (aerogel counters)

Item for TOF	Values
TOF1 counter size	$200 \times 25 \times 5 \text{ mm}^3$
TOF2 counter size	$700 \times 200 \times 20 \text{ mm}^3$
Average distance	2.5 m
Timing resolution ( $\sigma_t$ )	100 ps
$e^+$ efficiency ( $\epsilon_t$ )	99.9%
$\mu^+$ mis-identification	0.1%
TOF mass resolution	$\sigma = 1200 \text{ (MeV}/c^2)^2$
Item for AC	Values
Radiator (thickness)	Aerogel (20 mm)
Transmission length ( $l$ )	40 mm for $\lambda = 400 \text{ nm}$
Refractive index ( $n$ )	1.08
Radiator area	$220 \times 40 \text{ (mm}^2) \times 12$
PMT	R580
$e^+$ efficiency	99.88%

Table 7: Main parameters of the Pb-glass Cherenkov counter (PGC). One counter is installed in each gap.

Parameter	Value
Size (cm)	$70^H \times 20^W \times 10$ cm
Pb fraction	57 %
Density ( $\rho$ )	4.97 g/cm <sup>3</sup>
Weight	70 kg
Refractive index ( $n$ )	1.67
Radiation length ( $X_0$ )	2.33 cm
$e^+/\mu^+$ mis-ID	< 2%

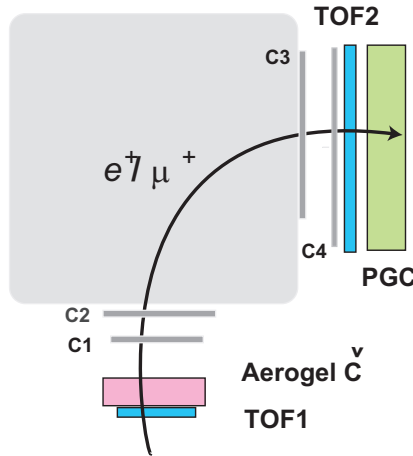


Figure 10: Schematic view of  $e^+/\mu^+$  discrimination, with the aerogel counter (AC), the TOF counters and the Pb-glass Cherenkov (PGC) counter.

good  $e^+/\mu^+$  discrimination. By combining this Pb-glass counter with the AC counter and/or TOF system, we can identify the charged particles with high precision.

### 4.2.3 PID efficiency calibration

It is clear that particle mis-identification introduces an additional uncertainty for the  $R_K$  determination. In order to check the performance of the particle identification by the TOF and AC system, the mis-identification probability will be directly measured using the experimental data, which is very similar method mentioned in Section 4.1. Here, the PGC system is available and it will help to confirm the particle identification for this calibration purpose. The probability of the  $e^+$  inefficiency and the  $\mu^+$  mis-identification by the AC counter can be measured by comparing the AC signals with the TOF and PGC information. It is to be noted that four-point tracking can be

Table 8: Summary of the performance check for the particle ID. The PGC detector plays a supplementary role in the PID probability measurements for the AC and the TOF systems. The PID probability can be determined by changing the combination of AC, TOF, and PGC.

Element for check	Tracking elements	PID
AC	C1, C2, C3, C4	TOF $\otimes$ PGC
TOF	C1, C2, C3, C4	AC $\otimes$ PGC
PGC	C1, C2, C3, C4	TOF $\otimes$ AC

used for this study. By changing the combination of the detectors and repeating the calibration, we can check the performance of all three detectors, as shown in Table 8. The systematic uncertainty due to non-ideal performance of the particle identification is subject to the statistical uncertainty of these efficiency determinations.

Here we will use the  $K_{e2}$  and  $K_{\mu2}$  events, and the statistical error of the efficiency determination is the same as the results obtained in Section 4.1. Assuming 1% mis-identification probability (namely 99% of trigger efficiency) and using the full data of the main run  $250 \times 10^3$  of  $K_{e2}$  events, the systematic uncertainty due to the non-ideal performance of the particle identification is expected to be controlled to a level 0.03% thus yielding

$$\Delta R_K/R_K = 0.00035, \quad (11)$$

following the procedure of Eq. (8) in Section 4.1.

As discussed in Section 3.3.3, the  $K_{e3}$  events obtained by changing the magnetic field of the spectrometer to  $B = 0.9$  T can be used for a quick efficiency check. We will have a periodic examination of the PID performance using the  $K_{e3}$  events during the experiment.

### 4.3 CsI(Tl) inefficiency

The uncertainty of the CsI(Tl) detector efficiency also affects  $R_K$ , since the measurement  $K_{l2\gamma}$  is done using this detector. Although the fraction of the relevant radiative decay (IB) is very small compared with the main peaks of  $K_{l2}$ , these effects are checked here. The influence is different for  $K_{\mu2\gamma}$  and  $K_{e2\gamma}$ . The recorded events are grouped into D0 and D1 as explained in Section 2. Of course the CsI(Tl) efficiency problem is related to the D1 events. The acceptance of the CsI(Tl) detector is determined by the following factors:

- The solid angle of the barrel. Since there are 12 "muon holes" plus the beam inlet and outlet, the solid angle is only about 75% of  $4\pi$ . This solid angle is dependent on the kaon stopping distribution in the target and its drifting or fluctuation during the measurement causes an error. (The effect of the kaon

stopping distribution is discussed later in Section 7 as one of the input parameter uncertainty in the simulation calculation.)

- The existence of the threshold energy,  $E_{th}$ , of the photon detection. According to the current design of the CsI(Tl) readout by means of avalanche diode (APD), the threshold energy should be about 7 MeV. The instability of the electronic circuits for  $E_{th}$  and the gain can cause an error.
- Clustering efficiency. In the clustering analysis of the hit crystal modules, we might lose some  $K_{l2\gamma}$  events in order to reject background and to treat pileup events. These characteristics are dependent on the beam intensity and the beam halo condition.
- As long as  $E_\gamma$  exceeds  $E_{th}$  and the photon hits the central part of the barrel (far from the "holes") we may assume that the inefficiency is zero.

#### 4.3.1 Effects on $K_{\mu2\gamma}$

The peak counting of  $K_{\mu2}$  events is not affected by the CsI(Tl) efficiency. The  $K_{\mu2\gamma}$  with the photon energy  $E_\gamma < E_{th}$  and about 25% (detector solid angle) of the  $E_\gamma > E_{th}$  are also grouped into D0 and suffer no CsI(Tl) efficiency problem. Only about 75% of them which are in D1 (it is about 0.1% of the peak) can be affected by the CsI(Tl) efficiency. The reason for the inefficiency due to the first bullet is now irrelevant, because the inefficient part simply shifts the events to D0. Thus, if we can suppress the fluctuation of the efficiency due to the second and third reasons below 1.0%, we can perform a measurement of  $\tilde{K}_{\mu2}$  with an accuracy better than  $1.0 \times 10^{-5}$ , which is negligible compared to the  $K_{e2\gamma}$  effect.

#### 4.3.2 Effects on $K_{e2\gamma}$

Regarding the  $K_{e2\gamma}$ , we can apply the same argument. In this case the radiative decay is dominated by SD which has a higher photon energy spectrum and the total strength is almost the same as the  $K_{e2}$  peak. The part of  $E_\gamma < E_{th}$  and about 25% of  $E_\gamma > E_{th}$  fall into D0 and is irrelevant to the CsI(Tl) efficiency problem. The IB fraction in D1 (which is known to be about 0.1% of the  $K_{e2}$  peak) suffers the efficiency fluctuation directly. However the IB fraction in D0 is evaluated by subtracting SD which is calculated from D1-SD with a scaling factor  $k \sim 0.45$  (see Section 6.2). The D1-SD is about 14% of the peak after applying the charged momentum cut  $p_e > 228$  MeV/c, and thus the D0-SD is 7% of the peak. Hence, if we can suppress the efficiency uncertainty to the level of 1.0%, we will achieve a D0-IB error of  $7 \times 10^{-4}$ , and a total uncertainty of  $\tilde{K}_{e2}$  is  $3.5 \times 10^{-4}$ . The total error in  $\Delta R_K/R_K$  is thus calculated to be

$$\Delta R_K/R_K = 0.0007. \quad (12)$$

In any case it is important to maintain a stable CsI(Tl) system by keeping the beam and the electronic conditions constant. The CsI(Tl) gain stability will be monitored with an LED and a Xe light source regularly as was done in E246.

#### 4.4 Trigger and DAQ

Events are accepted when the following trigger requirements are satisfied:

$$\check{C}_K \otimes TOF2, \quad (13)$$

where  $\check{C}_K$  is the multiplicity condition of the Cherenkov K-ring $>7$  and  $TOF2$  is the TOF2 counter hit.  $\check{C}_K$  is necessary to discriminate  $K^+$  from  $\pi^+$  by the beam Cherenkov counter. The  $TOF2$  requirement is to confirm that a charged particle has been transported through the spectrometer. A typical trigger rate is  $2 \times 10^3$  events/s. Since the PID information by the AC signal and the TOF measurement is not included as part of the trigger in the  $R_K$  measurement, we can remove any experimental bias based on particle mis-identification at the trigger level using the above open trigger condition.

A data taking rate of  $2 \times 10^3$  events/s trigger should be possible using present-days technology for a high-rate measurement. However, taking into account relatively high trigger rate, we will also prepare a back-up trigger scheme of

$$\check{C}_K \otimes TOF2 \otimes AC \oplus SC \cdot [\check{C}_K \otimes TOF2], \quad (14)$$

where  $AC$  is the aerogel Cherenkov counter hit and  $SC$  is pre-scaling rate. The  $K_{e2}$  decays are recorded by the former trigger and the AC detector efficiency can be determined from the  $K_{e2}$  events recorded by the latter trigger. Adopting the  $SC$  parameter to be 0.05, we can expect the trigger rate to be 100 triggers/s, which can be easily accepted using the existing DAQ resources in KEK. The number of the  $K_{e2}$  events obtained by the pre-scaled trigger is  $10 \times 10^3$  and the statistical uncertainty of the efficiency measurement is expected to be  $10^{-3}$  using the same procedure described in Section 4.1. It is to be noted that statistical loss of the  $K_{\mu2}$  events by the pre-scaled trigger is negligible. Needless to say the  $SC$  uncertainty should be better than  $10^{-3}$ .

Since the difference of the trigger response between  $K_{e2}$  and  $K_{\mu2}$  introduces a systematic uncertainty at the trigger stage, we should carefully check it before the data collection by inserting test pulses into the trigger system, as shown in Fig. 11. In particular, effects due to DAQ dead time, pile-up, unexpected second pulse creation, high rate counting, etc. should be examined. The output from a random pulse generator is divided into two signals, and one of them feeds the additional trigger unit where output pulses simulating the actual detector signals by the  $K_{e2}$  and  $K_{\mu2}$  decays can be generated. They are sent to the electronic modules for each detector element. The number of the test pulses before and after the trigger logic will be compared in order to confirm the correct response of the trigger logic. It is also important to investigate the rate dependence to check whether there is any dead time effect in the trigger efficiency.

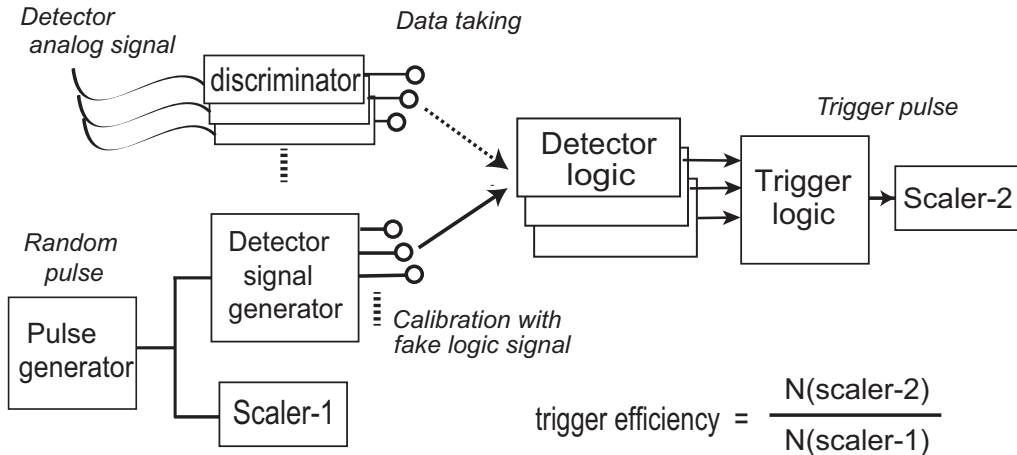


Figure 11: Schematic diagram for the trigger test. The difference of the trigger response between  $K_{e2}$  and  $K_{\mu2}$  can be checked by inserting test pulses into the trigger system. Outputs from the fake trigger logic simulate the actual detector signals.

## 5 Systematic errors from the measurement (2)

### –Errors due to due to backgrounds –

Systematic uncertainties can arise from backgrounds, which we categorize into two groups. One is the physics background associated with stopped  $K^+$  in the target, and the other is the background related to other beam particles. The latter is generally of accidental nature and is common to the  $K_{e2}$  and  $K_{\mu2}$  decays. We can reduce its effect by calculating the ratio  $N(K_{e2})/N(K_{\mu2})$ . we discuss the following major backgrounds in detail:

- muon decay in flight in  $K_{\mu2}$  decay,
- photon conversion in the radiative decay,
- accidental beam halo hits in the CsI(Tl) detector,
- accidental beam halo hits in the aerogel Cherenkov counters, and
- accidental events due to  $K^+$  to  $K^0$  conversion.

### 5.1 In-flight $\mu^+$ decay

$K_{\mu2}$  events with in-flight  $\mu^+$  decay ( $\mu^+ \rightarrow e^+\nu\bar{\nu}$ ) before reaching the AC counter are identified as  $K_{e2}$ . Although the AC will be placed as close as possible to the  $K^+$  stopping target, this background is not negligible and should be subtracted. Here, it is to be noted that the endpoint of the  $e^+$  momentum from the  $K_{\mu2}$  muon decay in flight (DIF) is the same as the  $e^+$  momentum from  $K_{e2}$  decay (247 MeV/c), as shown in

Fig. 12. Furthermore, since the endpoint corresponds to the forward boosted case, it is difficult to remove the events only by a momentum analysis. However, the fraction of these events is very small and most of the  $e^+$  from DIF have momenta much smaller than region of interest, as shown in Fig. 13 (a),(b). We are only interested in the decay positron region with momenta higher than 228 MeV/c, which is overlapping with the  $K_{e2\gamma}$  spectrum.

The fraction of muon DIF in the region before reaching the AC is

$$f \propto 1 - \exp(-l/\lambda) \quad (15)$$

where  $l$  is the average distance from the decay point to the AC, and  $\lambda$  is the decay length which is dependent on the muon momentum,  $\lambda = \beta\gamma c\tau = 1494$  m for  $p_\mu = 236$  MeV/c. The forward decay with the positron momentum range of  $p_{e^+} \geq 228$  MeV/c becomes a background beneath the  $K_{e2}$  peak and  $K_{e2\gamma}$  momentum distribution, which is calculated in a Monte Carlo calculation to be  $1.2 \times 10^{-3}$  of the total  $K_{\mu 2}$ . This fraction should be subtracted.

The error arises from the uncertainty of this subtraction due to the ambiguity of the effective length of  $l$ ; the boundary of the AC sensitive region is not yet known precisely. At the moment we regard 1/4 of the 2 cm AC radiator thickness ( i.e. 0.5 cm) to be the uncertainty in  $l$ , which yields a subtraction uncertainty of  $0.4 \times 10^{-5}$ . If we take into account the ratio of the  $K_{l2}$  branching ratios and the fraction of the relevant charged particle momentum spectrum, then we obtain

$$\Delta R_K / R_K = 0.00015, \quad (16)$$

which can be improved by understanding the details of the AC performance from a comparison of the test experimental data with the simulation.

## 5.2 $e^\pm$ creation from a radiated photon in $K^+ \rightarrow \mu^+ \nu \gamma$ decay

The photon conversion of  $K_{\mu 2\gamma}$  into  $e^+e^-$  mimics  $K_{e2}$  if the conversion occurs in a material before the AC. For example, an  $e^\pm$  generated in the TOF1 counter through which the  $\mu^+$  passes will make a signal in the aerogel Cherenkov counter, and the  $\mu^+$  which coincides with the generated  $e^\pm$  turns out to be identified as an  $e^+$  from  $K_{e2}$ . Figure 14(a) shows the  $e^\pm$  arrival probability,  $w(E_\gamma)$ , at the AC counter as a function of the original photon energy for all the directions and energies of the emitted  $\gamma$ . Figure 14(b) is the photon-energy distribution of the  $K_{\mu 2\gamma}$  decay, where the vertical axis is normalized so that the integration over the entire region is unity. Although the charged particle mass obtained from the TOF measurement indicates a muon and thus we can remove most such background, the imperfect TOF separation results in backgrounds. The number of those background events,  $N(K_{\mu 2\gamma}^{BG})$ , can be expressed with the TOF mis-ID probability  $\bar{\epsilon}_{TOF}$  as,

$$N(K_{\mu 2\gamma}^{BG}) = N(K_{\mu 2\gamma}) \cdot \bar{\epsilon}_{TOF} \int_{E_0} \Omega_{K_{\mu 2\gamma}}(E_\gamma) \cdot d\Gamma(E_\gamma) \cdot w(E_\gamma) \cdot dE_\gamma, \quad (17)$$

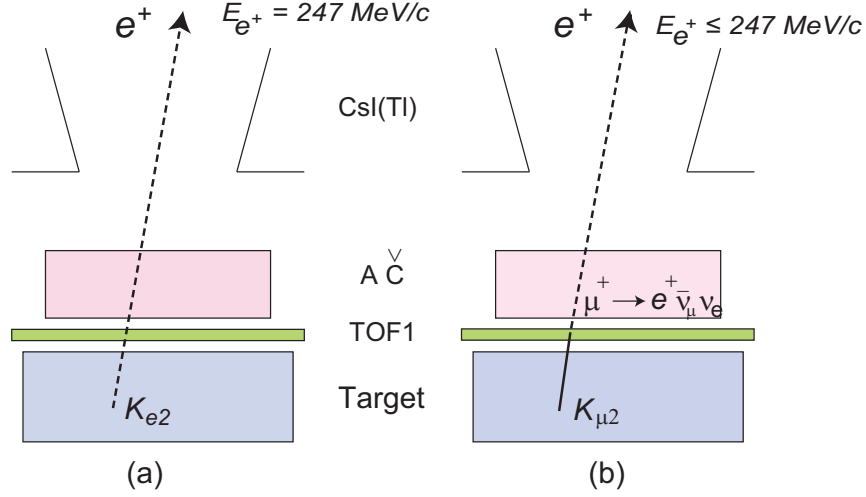


Figure 12: Schematic drawing of muon decay in-flight,  $\mu$  DIF, (right) compared with  $K_{e2}$  (left). The end point of DIF positron (for forward decays) is overlapping to the  $K_{e2}$  peak in the presence of finite momentum resolution. Also the  $e^+$  with  $p_{e^+} > 228 \text{ MeV}/c$  cannot be distinguished from  $K_{e2\gamma}$ , since they are almost in the forward direction. This fraction should be subtracted. However, an uncertainty arises from the ambiguity of the AC sensitive region entrance.

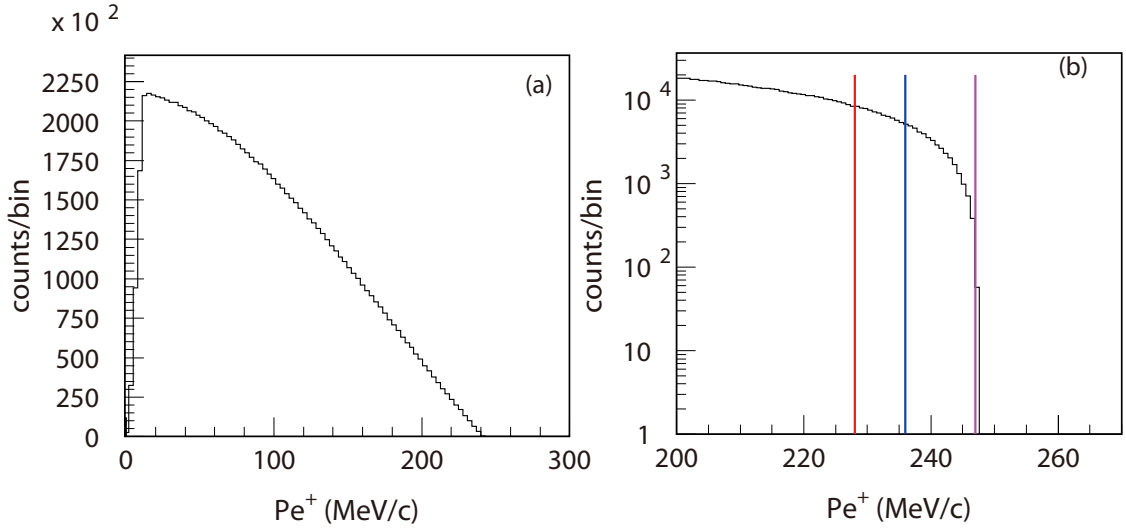


Figure 13: The  $e^+$  momentum spectra of in-flight  $\mu^+ \rightarrow e^+ \nu \bar{\nu}$  decay from the  $K_{\mu 2}$  decay reaching the muon holes: (a)  $e^+$  momentum in the whole range (linear scale), (b)  $e^+$  spectrum in the high-momentum region (logarithmic scale). The red, blue, and purple lines in (b) correspond to the  $K_{e3}$  endpoint, and the  $K_{\mu 2}$ , and  $K_{e2}$  lepton momenta, respectively. The admixing fraction of these events after requiring  $p_{e^+} > 228 \text{ MeV}/c$  is obtained to be  $1.2 \times 10^{-3}$  of the total  $K_{\mu 2}$ .

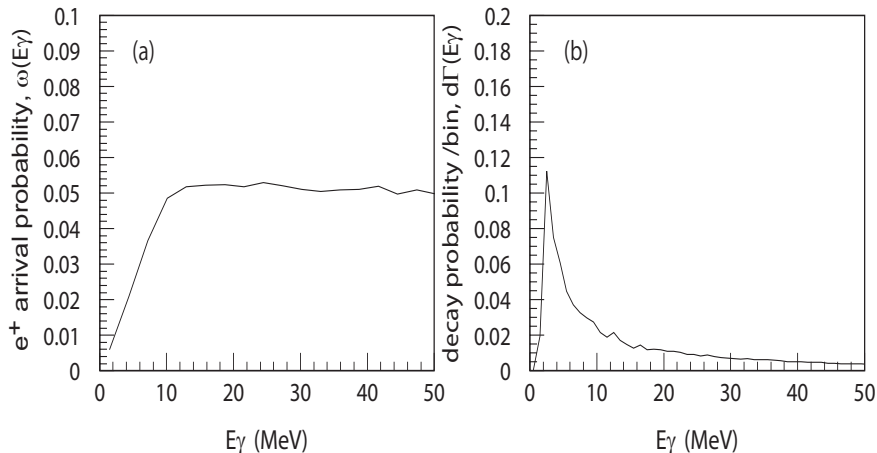


Figure 14: Panel (a) shows the  $e^\pm$  arrival probability,  $w(E_\gamma)$ , at the AC counter as a function of the original photon energy. Panel (b) shows the photon energy distribution of the  $K_{\mu 2\gamma}$  decay, where the vertical axis is normalized such that the integration over the entire region is 1. The fine structure in the spectra is due to statistical fluctuations.

where  $\Omega_{K_{\mu 2\gamma}}$  is the detector acceptance and  $d\Gamma(E_\gamma)$  denotes the differential decay width (or the photon-energy probability distribution normalized to 1). The lower bound of  $E_0 \sim 1.6$  MeV is chosen because the converted  $e^\pm$  can generate a signal in the AC. The  $K_{\mu 2\gamma}^{BG}$  fraction can then be obtained as  $N(K_{\mu 2\gamma}^{BG})/N(K_{e2}) = 2.2 \times \bar{\epsilon}_{TOF}$ . As discussed in Sec. 4.2, the  $\epsilon_{TOF}$  value can be directly measured using the experimental data. Here, assuming  $\bar{\epsilon}_{TOF} = 10^{-3}$ , the uncertainty is estimated to be

$$\Delta R_K/R_K = N(K_{\mu 2\gamma}^{BG})/N(K_{e2}) = 0.0002. \quad (18)$$

### 5.3 Accidental beam halo hit in CsI(Tl)

Accidental beam particle hits in the CsI(Tl) coincident with a  $K_{l2}$  may cause background events with additional statistical fluctuation. Although the central part of the detector near the beam axis is protected against an incoming second particle during the  $K^+$  decay period, the CsI(Tl) system with a larger radius is more exposed to the beam halo. When an otherwise D1 event is contaminated by such a " $\gamma$ ", it will be lost since we do not analyze events with more than two clusters in the CsI(Tl). As for the other D0 events, including the  $K_{l2}$  peaks, they only shift to D1<sup>n)</sup>, thus this does not affect the total number of events. The difference of event loss due to the former reason between  $K_{e2}$  and  $K_{\mu 2}$  produces a systematic error.

Since the number of  $K_{e2}$  event is far smaller, this mode is relatively more affected by the loss. If we denote the background hit rate in any of the CsI(Tl) crystals leading

<sup>n)</sup>Here we assume that no cut is set on the photon energy deposit in the CsI(Tl).

to loss as  $n(bg)$  and the time gate for an accidental coincidence as  $\tau_{acci}$ , the number of accidental BG events relevant to the loss is

$$N_{acci} = N(K_{e2\gamma} : D1) \cdot \tau_{acci} \cdot n(bg). \quad (19)$$

The relative statistical fluctuation of  $N_{acci}$  is thus  $1/\sqrt{N(K_{e2} : D1) \cdot \tau_{acci} \cdot n(bg)^{o)}$ . From our experience in E246 at the KEK-K5 beamline where the  $\pi^+/K^+$  ratio was 8-10, we can assume the background probability  $\tau_{acci} \cdot n(bg)$  should be smaller than 5% for the beam at K1.1BR, where the  $\pi^+/K^+$  ratio will be smaller than unity. Since we expect  $N(K_{e2\gamma} : D1) \simeq 40 \times 10^3$  <sup>p)</sup> we anticipate an error of  $\Delta N(K_{e2\gamma})/N(K_{e2}) \simeq 1.8 \times 10^{-4}$  corresponding to the final systematic error contribution of

$$\Delta R_K/R_K = 0.00018. \quad (20)$$

Fig. 15 shows schematically this kind of background. The incident accidental beam particle can also be a neutral particle which is not vetoed by B0 or coming outside of the beam region.

## 5.4 Accidental beam hits in the aerogel Cherenkov counters

Beam halo  $\pi^+$  particles ( $\simeq 500-800$  MeV/ $c$ ) at the K1.1BR beam line can generate a signal in the aerogel Cherenkov counter mimicking an  $e^+$ . If these  $\pi^+$ s accidentally coincide with a  $K_{\mu 2}$ , it might be counted as a  $K_{e2}$  event. Although such events can be basically rejected by requiring one cluster in the beam hodoscope B0, (which is located at the beam collimator of the K1.1BR beamline to record all particles during the  $K^+$  decay period with several lifetimes), and also by applying a TOF analysis to discriminate the mass, there may be some inefficiency  $\bar{\epsilon}_{veto}$  in B0 and probability of miss ID  $\bar{\epsilon}_{TOF}$  in TOF. The number of these backgrounds in  $K_{e2}$  ( $N_{acci}^\pi$ ) can be written as,

$$N_{acci}^\pi = N(K_{\mu 2}) \cdot \tau_{acci} \cdot n(\pi) \cdot \bar{\epsilon}_{veto} \cdot \bar{\epsilon}_{TOF}, \quad (21)$$

where  $\tau_{acci} \cdot n(\pi)$  is the  $\pi^+$  accidental coincidence probability determined from the time resolution  $\tau_{acci}$  of the AC counter and the background beam rate  $n(\pi)$ , We can assume  $\bar{\epsilon}_{veto}$  and  $\bar{\epsilon}_{TOF}$  to be  $10^{-2}$  and  $10^{-3}$ , respectively, as the performance target of these detector elements. Taking  $\tau_{acci} = 10$  ns and assuming  $n(\pi^+) = 2.2 \times 10^4/s$  hitting the AC counter we can anticipate  $N_{acci}^\pi = 2.2 \times 10^{-9}$  for an accidental counts<sup>q)</sup>. Since those events cannot be subtracted, we have to include them into the systematic error, namely

$$\Delta R_K/R_K = 0.0001. \quad (22)$$

<sup>o)</sup>The expression Eq. (15) in the Addendum 1 was misleading and the evaluation of  $\Delta R_K/R_K$  of Eq. (16) has been revised in this report.

<sup>p)</sup>Only 170 events from IB affect  $R_K$  directly, while the rest of the events from SD contribute indirectly in the D0-SD subtraction. Therefore the estimate of Eq. (20) is an overestimate on the safe side.

<sup>q)</sup>The evaluation of Eq. (31)-(35) in Addendum I were inaccurate and here revised in this report.

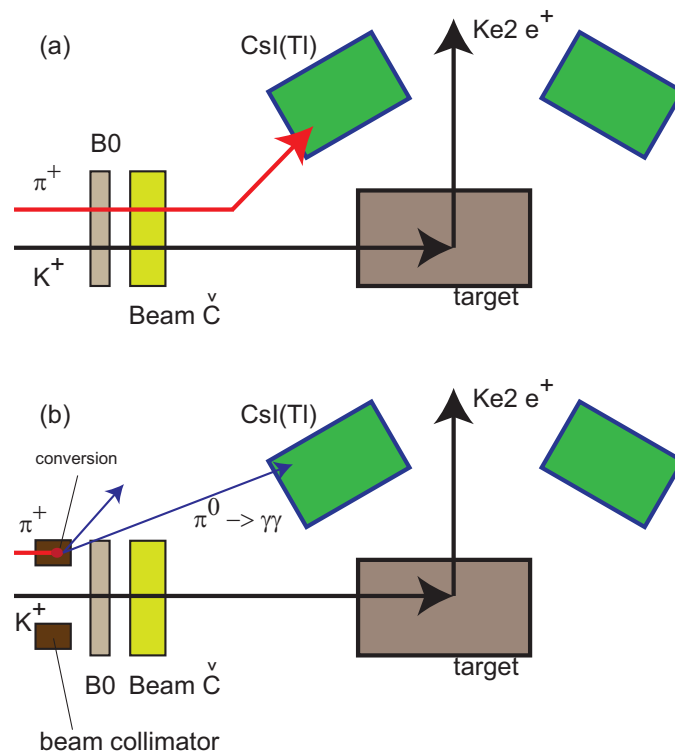


Figure 15: Schematic drawing of the background due to accidental beam halo hits in the CsI(Tl) detector. The second charged particle such as  $\pi^+$  are vetoed by the B0 hodoscope, but its inefficiency as well as neutral particles coming outside of B0 are responsible for this accidental background. (a)  $\pi^+$  scattering event and (b)  $\pi^+$  to  $\pi^0$  charge exchange event with one of the photons entering the CsI(Tl).

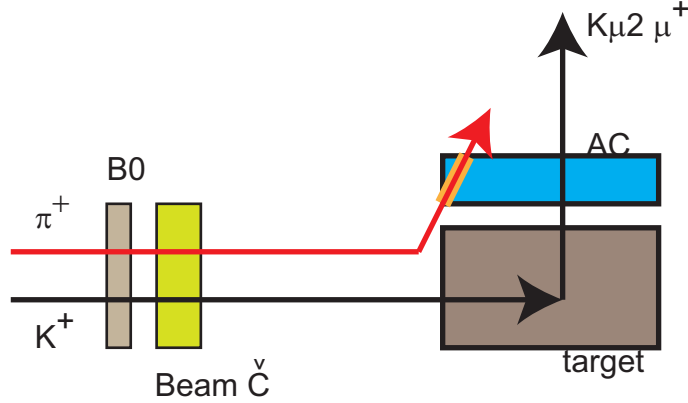


Figure 16: Schematic drawing of the background due to accidental beam halo  $\pi^+$  hit in the aerogel Cherenkov counter (AC). Although most of second incident particles are vetoed by the B0 hodoscope, its inefficiency together with the particle mis-ID in the TOF counter can cause the accidental background.

Fig. 16 shows schematically this kind of background. Although most of second incident particles are vetoed by the B0 hodoscope, its inefficiency together with the particle mis-ID in the TOF counter cause the accidental background.

### 5.5 Accidental events due to the $K^+$ to $K^0$ conversion

The  $K^+$  can be converted into a  $K^0$  through a charge exchange reaction during the  $K^+$  stopping process. This might give rise to a background. However, the  $K_L$  component is not accepted by the detector because of its long lifetime ( $\tau_{K_L} = 52$  ns). Also we can remove the  $K_S$  component with  $\tau_{K_S} = 90$  ps by rejecting the prompt events in the  $K^+$  decay time spectrum. ( We can remove effects from in-flight  $K^+$  decays by the same method. ) From the E246/470 experimental results, the peak width of the prompt events was obtained to be 0.5 ns in  $\sigma$ . Requiring the condition for the time difference between the beam Cherenkov counter and TOF1 to be  $\Delta_t > 2$  ns, the background fraction can be reduced to a level of 0.003% of the total  $K_{e2}$  and  $K_{\mu 2}$ , and therefore, the uncertainty can be reduced to

$$\Delta R_K / R_K = 0.00003. \quad (23)$$

This prompt cut, however, also rejects genuine  $K_{e2}$  and  $K_{\mu 2}$  events. Therefore, careful tuning of the cut point will be necessary in the analysis. Fig. 17 shows schematically how we can reject such a background.

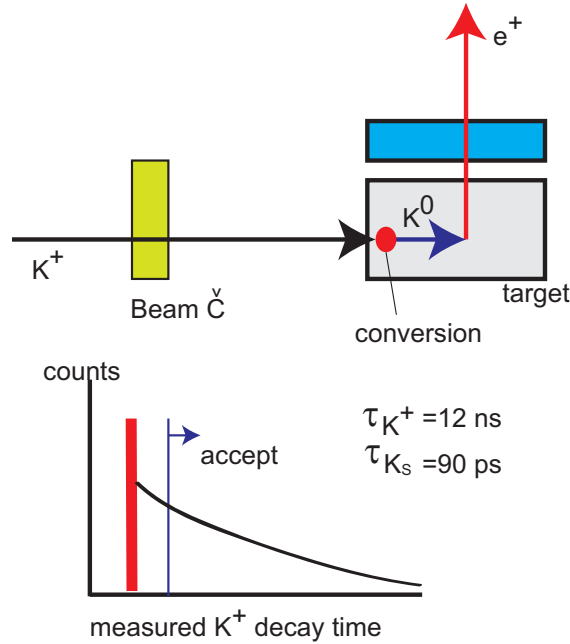


Figure 17: Schematic drawing of the background due to  $K^+$  charge exchange to  $K^0$ . By selecting only delayed events we may reject this type of background.  $K^+$  decay-in-flight events can also be removed.

## 6 Systematic errors from the measurement (3)

### —Analysis—

#### 6.1 Analysis code and cut parameters

In general the data analysis is a potential source of systematic error due to the imperfect algorithm and ambiguities in the event selection. In a precise experiment all the conceivable sources have to be checked. In the present experiment, however, the analysis is common to  $K_{e2}$  and  $K_{\mu3}$  up to PID in respect to charged particle tracking, photon detection of the radiative decays with the CsI(Tl) calorimeter, and second beam particle veto with the beam counters. Even if there are some imperfections in the analysis code, these affect  $K_{e2}$  and  $K_{\mu2}$  equally, and have no serious influence on the event number ratio. Needless to say we will test the analysis code thoroughly.

Regarding the PID and CsI(Tl) photon detection, the possible errors were discussed related to the detector performance. There is no other conceivable concern in the analysis itself. In principle the MC simulation calculation described in Section 3.3.1 for the detector acceptance estimate starts from the very beginning of the detector response generating real signals, so as to reproduce the actual experimental condition. The MC event selection parameters should be chosen the same as in the real analysis. The ambiguity associated with the simulated detector signals produces

only a small effect on the MC event selection.

As discussed before, the  $K_{e2}$  events have a long tail in the momentum spectrum due to the external bremsstrahlung in the kaon stopping target. Good  $K_{e2}$  events are extracted by setting a low threshold on  $p_\mu$  or high threshold on the photon energy, in order to avoid the  $K_{e3}$  momentum region. This cut parameter is considered to introduce the most largest systematic error in establishing good  $K_{e2}$  events. The error is related to the ambiguity of the external bremsstrahlung photon energy spectrum at the cut point, which arises from the uncertainty of the effective material thickness of the target for emerging  $e^+$ . Regarding this point a comprehensive estimate has been given in Section 7.3. In conclusion we regard the errors originating from the analysis code and cut parameters to be negligibly small compared to the SD subtraction error to be discussed next except for the  $K_{e2}$  low momentum cut.

## 6.2 Uncertainty of the SD component subtraction

In the present  $R_K$  measurement, the structure dependent component (SD) of the radiative  $K_{e2\gamma}$  decay becomes a background, which has to be subtracted from the analyzed D0 data sample as well as D1. The D0 sample also contains radiative events with a photon escaping from the calorimeter holes with relatively low rate, while the D1 sample contains SD events with significantly high statistics. Fig. 18(a) shows the anticipated distribution of the SD events in D1. In the case of D1, SD events are overlapping the IB events to a small extent. The subtraction of those SD events in the analysis leads to a source of error. Here, we also take into account the interference term of the IB and SD processes; however its INT effect is found to be negligible for the  $R_K$  determination.

The subtraction in D1 is straightforward. The SD component can be extracted by fitting its spectral shape and intensity with the two form factors of  $V + A$  and  $\lambda$  [10, 11].<sup>r)</sup> The error of the SD component (or IB component) in D1 is therefore solely a statistical one. The subtraction of the SD component in D0 is only possible by relying on the knowledge in D1, namely by using the obtained form factors and calculating the SD acceptance for zero-photon events in D0. This treatment is necessary because the acceptance ratio between D0 and D1 (defined as  $k$  later) is significantly dependent on the form factors. In this way the statistical error of the subtraction can be minimized. The error in D0 SD is thus caused by two factors:

- The uncertainty of the form factors to calculate the D0 SD acceptance,
- The statistical uncertainty due to the subtraction in D1.

In order to check the validity of this subtraction method and to estimate the errors, we performed a simulation study. SD events (40,000 as expected in P36) are

---

<sup>r)</sup>In the P36 proposal and addendums, the axial form factors in the  $K_{e2\gamma}^{SD}$  decay are described as  $F_V$  and  $F_A$ . On the other hand, the KLOE group adopted  $V + A$  parameterization, as described in Ref. [4].

Table 9: Results of simulation study

	D1	D0
MC generated SD events in D1	$4.0 \times 10^4$	-
IB events	170	-
Fitted $\lambda$	$0.395 \pm 0.012$	-
Acceptance ratio $k$	-	$0.45329 \pm 0.00043$
Event number in D0	-	$18,132 \pm 90 \pm 6$
Error of IB numbers	3	90
Relative acceptance of IB to $K_{e2}$ <sup>s)</sup>	0.0007	0.005
Contribution to $\Delta R_K/R_K$	-	0.00036

generated in D1 and superposed with the corresponding IB events which are about 170 from the acceptance comparison, as shown in Fig. 18(a). There are 10 IB events overlapping the SD events. This Dalitz plot was fitted with the  $\lambda$  form factor. For the event generation, the currently known form factors [4]<sup>s)</sup> were used. The  $\chi^2$  distribution is shown in Fig. 18(b) as a function of the  $\lambda$  parameter. The minimum reduced  $\chi^2$  value is 1.4 and the red circle in Fig. 18(b) corresponds to the assumed value in the simulation. The obtained results is

$$\lambda = 0.395 \pm 0.012 \quad (24)$$

with  $N(D1, SD) = 40,000 \pm 200$  and  $N(D1, IB) = 170 \pm 13$ . By using these obtained values the acceptance ratio  $k$  and  $N(D0, SD)$  are calculated as,

$$\begin{aligned} k &= 0.45329 \pm 0.00034 \\ N(D0, SD) &= 18,132 \pm 90 \pm 6. \end{aligned} \quad (25)$$

The error of  $N(D0, SD)$  involves both the statistical origin of  $N(D1, SD)$ ,  $\pm 90$ , and systematic origin of the form factors,  $\pm 6$ . At the moment (in this report), we are only interested in the error estimate, and the determination errors of  $N(SD)$  are only important; the central values of  $V + A$ ,  $\lambda$ ,  $N(D0, SD)$  and  $k$  are irrelevant<sup>t)</sup>. Also the form factor input for the event generation does not affect the results of errors significantly. By using the obtained errors of  $N(D1, SD)$  and  $N(D0, SD)$  and the acceptance ratio of IB to the main  $K_{e2}$  peak, we conclude the error associated with the SD subtraction to be,

$$\Delta R_K/R_K = 0.00036. \quad (26)$$

<sup>s)</sup>KLOE group reported the central value of  $\lambda = 0.38$  [4].

<sup>t)</sup>It was checked that the central values do not affect the error of  $k$  or  $N(D0, SD)$  significantly in the currently interested region.

<sup>s)</sup>The acceptance for IB is obtained with the condition of  $E_\gamma > 7.5 MeV$  and  $\theta_{e\gamma} > 2^\circ$ .

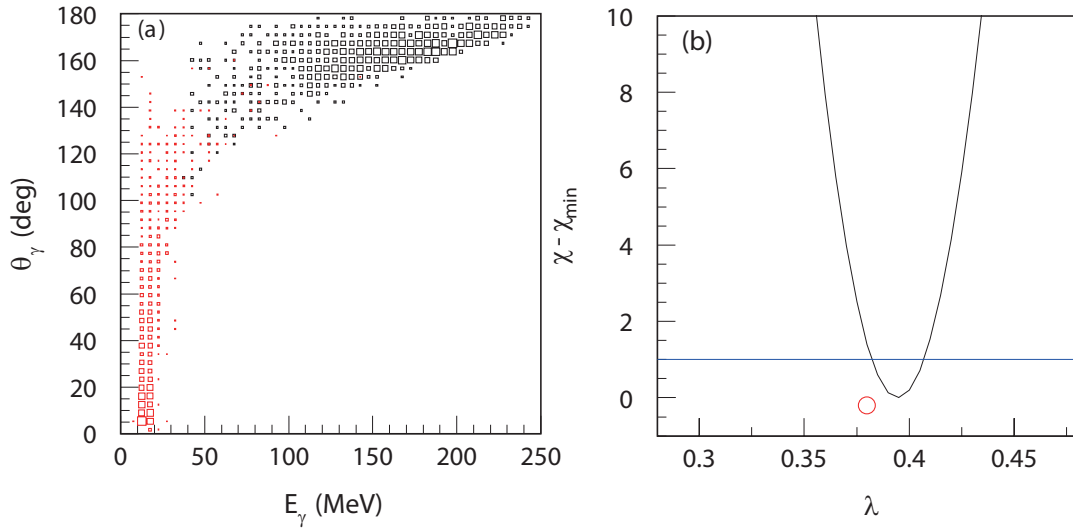


Figure 18: (a) The expected D1  $K_{e2\gamma}^{SD}$  events in the  $R_K$  measurement obtained by assuming these form factors in the simulation.  $K_{e2\gamma}^{IB}$  (red) and  $K_{e2\gamma}^{SD}$  (black) spectra stored in the simulated D1 sample: correlation plot for  $E_\gamma$  and  $\theta_{e+\gamma}$ , for SD (black) and IB (red). The events due to the IB and SD processes have a distinct structure and it is possible to separate them. (b) The  $\chi^2$  distribution as a function of the  $\lambda$  parameter. The minimum reduced  $\chi^2$  value is 1.4 and the red circle corresponds to the assumed value in the simulation.  $\chi^2$  distribution for the form factors are artificially determined by minimizing the difference between the expected  $K_{e2\gamma}^{SD}$  events in the  $R_K$  measurement and the same simulation events with much higher statistics.

## 7 Systematic errors in the MC simulation

In this section we will summarize the errors coming from the MC simulation. Since the decay width ratio  $R_K$  is derived by dividing the event number ratio  $N(\tilde{K}_{e2})/N(\tilde{K}_{\mu2})$  by the detector acceptance ratio  $Q = \Omega(\tilde{K}_{e2})/\Omega(\tilde{K}_{\mu2})$ , and this acceptance ratio is solely relying on MC simulation up to the check by using the experimental data, the errors of the MC simulation must be included in the sources of the final systematic errors of  $\Delta R$ . In the following we discuss and check every step of the simulation.

### 7.1 Acceptance estimate

#### 7.1.1 Acceptance

In Section 3, we presented three possible methods to estimate the ratio of the detector acceptance for  $K_{e2}$  and  $K_{\mu2}$  and showed the estimated size of the error wherever possible. Here we repeat them again for completeness.

1. Regarding the method of Section 3.3.1, we cannot say anything more than we presented in the previous Addendum. Based on the correctness of the MC code verified in the E246/E470 experiments using almost the same detector, we will try to reproduce all the observables such as the  $K_{\mu3}$  and  $K_{e3}$  momentum spectra and opening angles. We will also include the acceptance ratio, which, unfortunately, we are not able to check directly using the data. We will try to achieve the simultaneous reproducibility of the experimental data with an accuracy of 0.1 % by taking advantage of very high statistics of the P36 data.
2. As one of the possible check of the acceptance ratio using data we proposed the use of  $K_{\mu2}$  decay. As long as we achieve a measurement of momentum spectra without constant BG beneath the peak, the only concern is the uncertainty in the field effect correction  $\beta$ . Any possible bias in the correction can be checked at low field excitation where the field distribution is nearly dipolar. A 3D magnetic field calculation is currently underway. We must wait for tracking simulations using the calculated field distribution before we can include an error coming from  $\beta$ . We expect that the error due to the beam normalization  $n$  should be small, although not negligible.
3. We believe that the third method using  $K_{\mu3}$  decay is most promising, since the calibration process is contained only in the  $K_{\mu3}$  momentum spectrum. As discussed in Section 3.3.3, the error arises from:
  - the statistical error of the  $K_{\mu3}$  data,
  - the correction for the CsI(Tl) acceptance of the photon detection,
  - the magnetic field non linearity correction  $\beta$ ,
  - the form factors of the  $K_{\mu3}$  decay, and

- the application of the target energy loss in the simulation.

Regarding the first point the accuracy will be ensured by the high  $K_{\mu 3}$  event rate in a special control run. The necessary event number is provided by the demonstration using the existing E246 data. Regarding the second point we are primarily dependent on the event statistics, which can be sufficiently high. For the third point we can apply the same argument as in 2). Hence, we may conclude at the moment that the most dominant error in this method comes from the uncertainty of the  $K_{\mu 3}$  form factors as was discussed. The estimate of the acceptance ratio error is based on the current knowledge of the form factors. This and the contribution from the energy loss correction together gives us 0.00078.

### 7.1.2 Magnetic field

In general inaccuracy in the field mapping produces an error. Regarding the tracking, however, we use the same map for experimental tracking as well as the simulation. Furthermore the effect of a "bad field mapping" deteriorate only the momentum resolution. As long as the  $K_{e2}$  and  $K_{\mu 2}$  peaks are isolated, this fact does not introduce any bad effects on the event selection<sup>u)</sup>.

The only concern is the field distribution used in the acceptance ratio estimate discussed in Sec. 3.3.1, Sec. 3.3.2, and Sec. 3.3.3. However, the error in  $\beta$  due to an uncertainty in the field distribution should be small; this effect can be regarded as producing only a limited error on the final result. A more detailed investigation will be done after the completion of the field calculation.

## 7.2 Input parameters

The MC simulation has a number of input parameters. In general the uncertainties of these parameters produce an error in the acceptance estimate. There is however only one essential input condition in the simulation other than the detector geometry inputs, which were proven to be sufficiently accurate in the past calculations for E246/E470. It is the kaon stopping distribution in the target, from which the decay event generation starts. We might be able to start from a realistic beam condition, but the reproducibility of the real stopping distribution is not so convincing. Moreover, the real beam condition can be easily different from run to run. In the following we show the influence of the uncertainty of the kaon stopping distribution in the MC simulation and give an upper-bound of the error.

---

<sup>u)</sup>The only concern about the bad momentum resolution is the separation of the peak of  $K_{e2}$  and its radiative decay tail. However, as long as we count the peak and the tail together, it does not matter. The subtraction of the nuon in-flight-decay background (Section 5.1) has to be done taking into account the finite resolution.

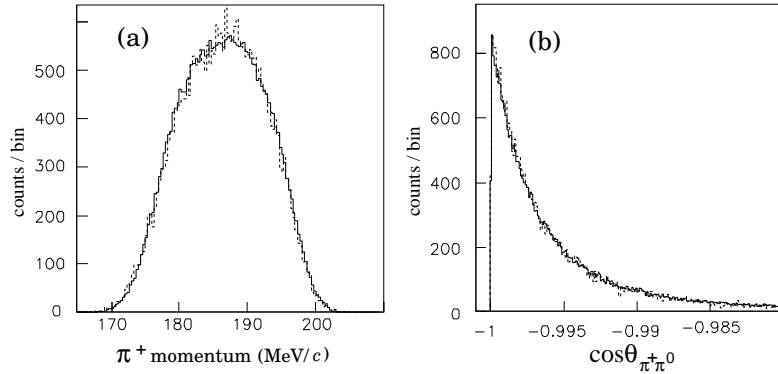


Figure 19:  $K_{\pi^2}$  spectra measured in the E246 experiment [5]. (a) is the  $\pi^+$  momentum without any energy loss correction in the target. (b) is the opening angle between the  $\pi^+$  and the  $\pi^0$ . The solid and dotted lines are the experimental data and the Monte Carlo simulation, respectively. The reduced  $\chi^2$  is (a) 1.07 and (b) 0.96

### 7.2.1 Effect of kaon stopping distribution ambiguity

The kaon stopping distribution in the target is the only physics input of physical experimental condition in the simulation calculation. It is determined by the beam characteristics and therefore can be time-wise changing. It is needless to say that the detector acceptance depends on this distribution significantly, and a slight shift might cause an error. The distribution will be prolonged in the beam direction due to finite momentum bite of the beam. The distribution is measured primarily by the tracking of incident kaons with the target fibers and tracing-back of decay charged particles, but with a finite resolution. The measured distribution is confirmed by fitting some spectra of physics observables. This can be done by using  $K_{\pi^2}$  decay, since two body decay kinematics is the best tool to do this. We demonstrate this method in E246. As shown in Fig. 19, the opening angle between  $\pi^+$  and  $\pi^0$  as well as the momentum spectrum of  $\pi^+$  could be fitted quite well with small  $\chi^2$  values.

However, we have to admit a certain ambiguity of the measured/fitted distribution due to the position resolution and fitting limit. Among the three coordinates,  $x$  and  $y$  are not very relevant to the acceptance. We have to consider the shift of  $z$  coordinate. If we parameterize the distribution to some function, we have to satisfied with the best accuracy of  $\delta z=0.5$  cm. According to a simulation calculation, this shift produces an acceptance change of 0.00015. Although we may expect a cancellation between  $e^+$  and  $\mu^+$ , we take this value as the contribution to the systematic error based on the safe-side estimate, as

$$\Delta R_K/R_K = 0.00015. \quad (27)$$

<sup>r)</sup>See the argument in Section 3.3.2.

Table 10: Major input parameters in the simulation calculations and their effects of the uncertainties on  $Q$  and  $R_K$ . The detector performances was assumed to be 100% in the simulation, but treated as the systematic error in the measurement.

Item	Uncertainty	Effect on	Proven in	$\delta R_K/R_K$
Detector geometry	small	$Q$	E246/470	$\ll 0.001$
Magnetic field	finite	$Q$	3D calculation	not known yet but $< 10^{-4}$ r)
$K^+$ distribution	large	$Q$	$K_{\pi 2}$	0.00005
Detector performance	assumed none	—	—	errors in $N(K_{l2})$

### 7.3 Interactions of emitted particles in the target

The interaction of the  $e^+$  and the  $\mu^+$  with the target material must be simulated accurately, since the interactions affect the yields of  $K_{e2}$  and  $K_{\mu 2}$  in several ways. There are three kinds of interactions:

1. Bremsstrahlung which is relevant to light positrons  $e^+$ ,
2. Annihilation in flight which is solely relevant to positrons, and
3. Conversion of photons in the radiative decays.

The particles also suffer from ionization and multiple scattering with the consequence of energy loss and angle smearing. Those effects have been treated elsewhere (in Section 3) as one of the influences on tracking performance causing a spectrometer acceptance change. The points 1) and 2) lead to a loss of  $K_{e2}$  events due to positron momentum threshold cut (in the case of 1)) or positron disappearance (in the case of 2)). The photon conversion, 3) , modifies the radiative decay strength in both decays (Section 5.2).

The probabilities of these interactions can be evaluated with a simulation calculation and corrected for in deducing the  $K_{e2}$  and  $K_{\mu 2}$  yields. The simulation calculation will be performed using the experimentally measured kaon stopping distribution. The ambiguity of the corrections gives rise to a systematic error. Since all these three interactions have constant probability for unit material length, the simulation errors are related to the ambiguity of the length of particle penetration in the target in two ways:

- the uncertainty of the kaon stopping point or decay vertex point,
- the inaccuracy of the material thickness input of the target.

Regarding the first point, the decay vertex determination will be done by the experimental data combination of decay positron tracking (with chambers and target fibers),

and maximum energy deposit by the incident stopping kaon. The average error of the penetration length due to this effect is discussed in the next subsection. With regards to the second point, we need a thorough investigation of the various materials and their thickness in the scintillating fiber target and the TOF counter(Section 7.3.2).

### 7.3.1 Error due to decay vertex resolution

Although we will use all the available data to determine the decay vertex, the kaon stopping point resolution is essentially determined by the size of the target fiber, which is  $3 \times 3 \text{ mm}^2$ . Since the kaon stopping points has a distribution, the real kaon stopping distribution in each  $3 \times 3 \text{ mm}^2$  fiber has to be taken into account in the simulation calculation. The fibers at the stopping distribution edge have to be treated carefully, because the acceptance of those fibers is slightly larger for the nearest gap among twelve gaps. This fact might give rise a bias in the penetration length estimate. Here we discuss two possible ways to take this into account.

- For each generated event in the simulation we attach a kaon stopping position in the  $3 \times 3 \text{ mm}^2$  fiber randomly according to the distribution function extracted from the global distribution in the total target. For a large number of generated events the ambiguity of penetration length in the target due to the uncertainty of the real stopping point in the fiber should be smeared out and the error of estimated average penetration length should be negligibly small. The only source of the error comes from the inaccuracy of the distribution function for simulation which is extracted as a function of fiber center coordinate. (Fig. 20 show this situation.) However, since the simulation distribution is generated realistically based on this fiber center coordinate function, there should be no mean penetration length difference in the first order.
- In order to give an upper bound for this error prior to the experiment, we have performed a model calculation assuming a simple kaon stopping distribution. If we input the fiber center coordinate into the penetration calculation, the average bias to the simulation calculation can be calculated to be less than 0.1 mm in the scintillator material. However, if we apply a more realistic distribution function the error should be much smaller. The error in the probability for the three interactions is summarized in Table 11.

We estimate the error to be

$$\Delta R_K/R_K = 0.00041. \quad (28)$$

### 7.3.2 Error due to material thickness uncertainty

The target and the TOF1 counter consist of several materials: plastic scintillator(1), optical isolation paint(2), partially supporting cylinder(3), and wrapping materials(4).

Table 11: Uncertainty of the probability for three interactions due to the finite target fiber size of  $3 \times 3 \text{ mm}^2$ .

Interaction	Probability uncertainty
Bremsstrahlung for positrons	0.038%
Annihilation for positrons	$\leq 0.010\%$
Photon conversion for both decays	0.010%
Total	0.041 %

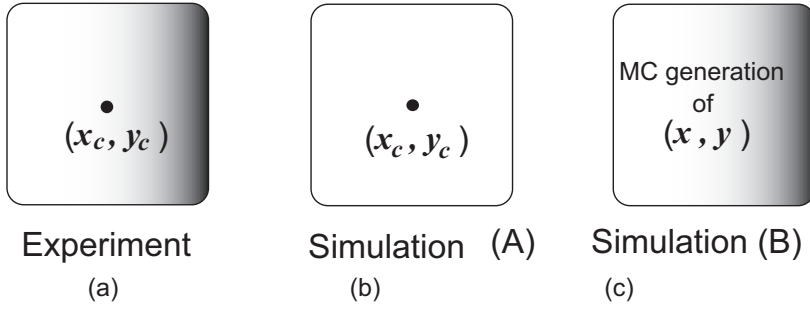


Figure 20: From the experiment we deduce a global  $K^+$  distribution function as function in terms of fiber center  $(x_c, y_c)$  (a). The fiber center is not the center of gravity of the  $K^+$  stopping in the fiber, if there is a gradient. If we use the center coordinate to generate events in the simulation (b) it makes an offset, which cannot be compensated among the 12 gaps. We perform an exact simulation calculation, taking into account the realistic distribution in each fiber (c). In this case the  $e^+$  penetration length distribution is exactly reproduced.

All the materials are input in the simulation calculation. Their nominal thicknesses are shown in Table 12. The thickness of the supporting cylinder and the TOF1 counter can be machined with high precision and the final measurement will be done (it is now under production) accurately; therefore we do not have to worry about the thickness error. As for the scintillator fibers and the reflecting paint layer, the thickness control in the production is not very easy and we have to anticipate some errors in their total thickness. We have already prepared about 500 fibers with painted reflective surfaces and an imbedded 1mm diameter wave length shifting fiber for light readout. The actual sizes of these fibers have been carefully measured, showing the distribution of Fig. 21. Out of these 500 pieces we will select 256 fibers with relatively uniform thickness and assemble the fibers as shown (Fig. 22). The overall ambiguity of the material thickness in the target is summarized in Table 13.

Table 12: Material thickness in the target (Specifications).

Material	Thickness	Relative error
Scintillating fiber	3.0 × 3.0 mm	±7 %
Paint (TiO <sub>2</sub> )	50 μm	±50 %
WLS fiber (Y11)	1.0 mm in diameter	±10 %
Glue	0.05 g/fiber-cm	±50 %
End Region Al tube	1.0 mm thicknes	0 (will be measured)
End Region Acryl ring	Complicated shape	0 (will be measured)
Cover (Polyvinyl fluoride)	50 μm ( $\rho=1.37-1.72$ g/cm <sup>3</sup> )	≈ 0
TOF1	5.0 mm	0 (will be measured)
Wrapping of TOF1	50 μm	±60%

Table 13: Estimated overall uncertainty of material thickness.

Material	Thickness uncertainty	
	(g/cm <sup>2</sup> )	( $X_0$ )
Scintillator	0.08	$1.8 \times 10^{-3}$
Paint	0.01	$6 \times 10^{-4}$
WLS fiber + glue etc.	0.04	$9 \times 10^{-4}$
Wrapping	0.02	$5 \times 10^{-4}$
Total	0.09	$2.2 \times 10^{-3}$

### 7.3.3 Error estimate

The error due to the corrections for these three interactions (bremsstrahlung, annihilation and photon conversion) was evaluated with the uncertainty of the material thickness (Table 14). The  $K_{e2\gamma}$  events with large photon energy are rejected by the  $p_e$  momentum cut of  $p_e > 228$  MeV/ $c$ . Its fraction is about 3.8%. The ambiguity of this fraction due to the material thickness uncertainty of  $2.2 \times 10^{-3} X_0$  is 0.3%. The  $e^+$  annihilation ambiguity which is also relevant to  $K_{e2}$  leads to only a small error. The probability of photon conversion, which decreases the radiative decay event rate is common to both channels; therefore, only the difference of the radiative decay fraction (it is about 1%) makes an effect. In total the error due to the bremsstrahlung is dominant and

$$\Delta R_K / R_K = 0.0002. \quad (29)$$

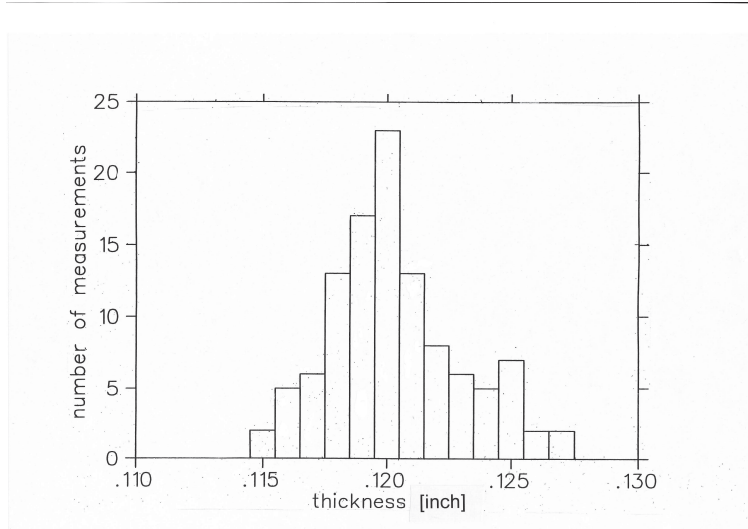


Figure 21: Distribution of the sizes of the 500 prepared scintillating fibers. The mean value is  $0.1203'' = 3.056$  mm. The standard deviation is 0.069 mm. We will select 256 fibers from the central part of the distribution for our target.

### 7.3.4 Other materials outside the target and associated error

The materials before entering the spectrometer magnet introduce necessary corrections due to the three interactions. They are the TOF1 counter, the aerogel Cherenkov counter and the GEM wire chamber. These counters can be measured accurately; hence the simulation input will be accurate and they will provide no significant errors.

## 7.4 Internal bremsstrahlung theory

The radiative correction is a higher order QED effect through the IB component of the radiative  $K_{e2\gamma}$  process, which is theoretically calculable. It contributes to the  $R_K$

Table 14: Errors due to the interaction correction. The bremsstrahlung and annihilation remove only  $\tilde{K}_{e2}$ , while the photon conversion affect both contributing to  $\Delta R_K/R_K$  with the difference of radiative decay fraction.

Interaction	Relevant to	Correction error	$\Delta R_K/R_K$
Bremsstrahlung (rejected)	$\tilde{K}_{e2}$	0.003	$2 \times 10^{-4}$
Annihilation in flight	$\tilde{K}_{e2}$	$\ll 10^{-4}$	$\ll 10^{-4}$
Photon conversion	$K_{e2\gamma}, K_{\mu2\gamma}$	$3 \times 10^{-3}$	$\sim 10^{-5}$
Total			$2 \times 10^{-4}$

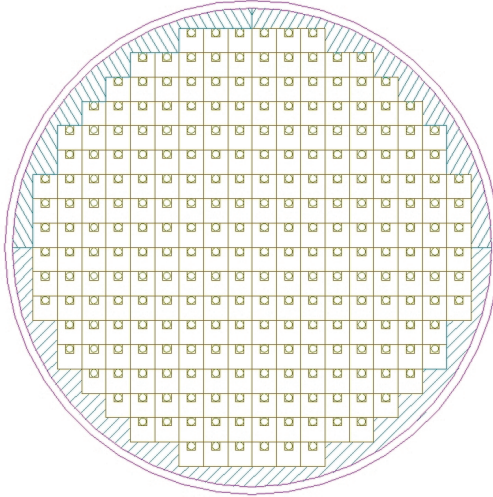


Figure 22: Cross section of the scintillating fiber target with 256  $3\times 3$  mm scintillation fibers read by WLS fibers with 1.0 mm diameter imbedded in a groove in each fiber. The 200 mm long fiber bundle is bound by two Acryl rings (shown in blue ) which are 30 mm long at each end. A 1 mm thick Al pipe also supports the target for 30mm at the DS end.

measurement as a correction factor indicated as the  $\delta$  term in Eq. (2). Since the IB process recorded in the D1 sample can be easily separated from the SD process because of their distinct spectral shapes, as shown in Fig. 18, we can check the theoretical calculation [12] by comparing with the experimental IB spectra, setting a particular threshold photon energy. The theoretical uncertainty can be estimated from the experimental reproducibility by the Monte Carlo simulation. Here, we estimated that the number of the accepted IB events is 170 taking the threshold photon energy of 7 MeV, while only spectra shape of the IB process was discussed in the previous Addendum I.

One of the main problem in treating radiative decays is the presence of the infrared divergence. The total decay width for single photon emission becomes infinity, while we can be compute it at any fixed order in  $\alpha$ . However, the problem of infinite probabilities can be solved [12] by extending the soft-photon approximation [13] to the whole energy range. The systematic uncertainty can be further reduced by using the full  $O(p^4)$  calculations for the amplitudes. Here, it should be emphasized that the contribution from the radiative correction was estimated to be negligible in the latest results reported by the NA62 group [3]. We estimate the small systematic uncertainty as

$$\Delta R_K/R_K \ll 0.001. \quad (30)$$

## 8 Summary

### 8.1 Summary of systematic error

In this report we have surveyed all the potential sources of systematic errors in the lepton universality measurement in P36 and estimated their size. Although we are still analyzing some errors (e.g. the error arising from the uncertainty of the B field distribution in the spectrometer ) we believe that we have included all the main sources. There are of course several errors which can only be analyzed using the real data. However, we can conclude at this moment that the total size of the estimated systematic error (which is the quadratic sum of each contribution.) is  $1.5 \times 10^{-3}$  for  $\Delta R_K/R_K$  and we are planning a run time to achieve a statistical error of  $2 \times 10^{-3}$ . Of course we have to make every effort to realize the conditions assumed in these error estimates. However, we regard the goal of the systematic error to be quite feasible to achieve.

Table 15: Summary of systematic errors

Error source	$\Delta R_K/R_K$	Comment	Addendum 1
<b>(1) Detector performance</b>			
Chamber efficiency	0.0004	Method-1	0.00035
PID performance	0.00035	$K_{e2}/K_{\mu2}$ run	0.00035
CsI(Tl) performance	0.0007	Ambiguity of efficiency	—
Trigger and DAQ	small	to be measured	—
<b>(2) Background</b>			
Muon decay in flight	0.00015	Distance to AC	0.00025
Photon conversion	0.0002		0.0002
CsI(Tl) beam hit	0.00018		0.0004
AC beam hit	0.0001		< 0.0001
$K^+$ conversion	0.00003		< 0.0001
<b>(3) Analysis</b>			
Code and cut parameters	small	$\ll 0.001$	—
SD subtraction	0.00036		0.00036
<b>(4) MC simulation</b>			
Acceptance ratio	0.00078	based on E246	—
Magnetic field	small	< 0.0001	—
Input parameters	small	$\ll 0.0001$	—
Kaon stopping distribution	0.00015		—
Target interactions	0.0004		0.0002
Material thickness	0.0002		—
IB theory	small	$\ll 0.001$	—
Total	0.0015		0.0013

## 8.2 Control and calibration runs

In order to achieve the required systematic errors, we will have to perform several control and/or calibration runs with the beam, as has been proposed for each item. Some of them (the  $K_{e3}/K_{\mu3}$  runs) can be combined. Table 16 summarizes these runs. Compared with the run time of the main data taking, the length of these runs (one week in total) is relatively long. However, they are definitely necessary for such a high precision experiment.

Table 16: Summary of planned calibration runs

Calibration	Field (T)	Trigger	Run time
Acceptance ratio with $K_{\mu2}$	1.34	$\mu^+$	1 day
Acceptance ratio with $K_{\mu3}$	0.9	$\mu^+$	1 day
Chamber efficiency	1.4, 0.9	$e^+, \mu^+$	5 days
PID efficiency	1.4, 0.9	$e^+, \mu^+$	included in 5 days
TOF counter efficiency	1.4, 0.9	$e^+, \mu^+$	included in 5 days
Trigger and DAQ	—	fake- $e^+, \mu^+$	off beam

## 8.3 Conclusion

In conclusion, we expect to achieve a sensitivity of  $\Delta R_K/R_K = 2.5 \times 10^{-3}$  in the search for violation of lepton flavor universality in the P36 experiment with the estimated errors of

$$\begin{aligned} \Delta R_K/R_K(\text{statistical}) &= 2.0 \times 10^{-3}, \\ \Delta R_K/R_K(\text{systematic}) &= 1.5 \times 10^{-3}. \end{aligned}$$

In Table 17, our target sensitivity is compared with the current experimental situation. NA62 reported this year (2011) their result from the whole data taken by 2007. Their systematic error is  $\Delta R_K/R_K = 0.0028$ , of which main contribution comes from the  $K_{\mu2}$  background, and the statistical error is also 0.0028 balanced to the systematic error.

P36 aims for a higher systematic sensitivity than the statistical one. This retains the possibility to improve the statistical accuracy in the future after confirming the systematic error level foreseen in the current analysis. Hence, we believe that it is worthwhile to perform P36 at J-PARC using a stopped kaon method which has completely different systematics from the in-flight-decay experiments of KLOE and NA62, as shown in Fig. 23.

Table 17: Comparison of the P36 sensitivity with the current experimental limits

Experiment	$R_K[10^{-5}]$	$\Delta R_K(stat)[10^{-5}]$ $\Delta R_K(stat)/R_K$	$R_K(syst)[10^{-5}]$ $\Delta R_K(syst)/R_K$	$\Delta R_K(total)[10^{-5}]$ $\Delta R_K(total)/R_K$
KLOE (2009)	2.493	0.025 0.0100	0.019 0.0076	0.031 0.011
NA62 (2011)	2.488	0.007 0.0028	0.007 0.0028	0.010 0.0039
World average	2.488			0.009 0.0036
P36 (2015?)		0.005 0.002	0.0038 0.0015	0.0065 0.0025
Theory (SM)	2.477			0.001 0.0004

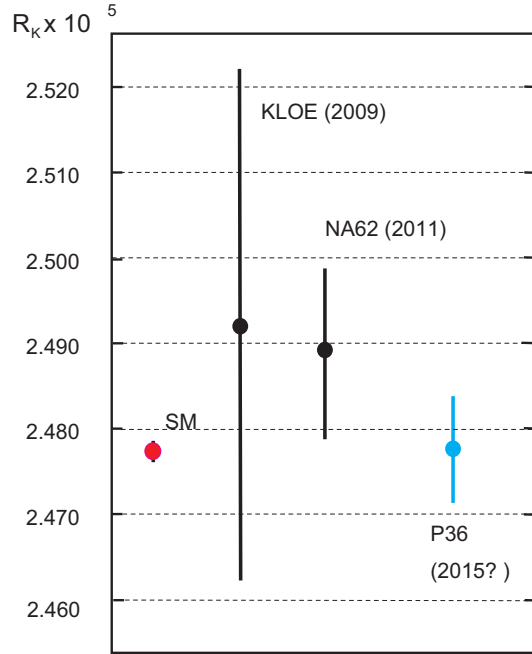


Figure 23: Status of  $R_K$  experiments. KLOE and NA62 are in-flight-decay experiments, whereas P36 is a stopped beam experiment. The central value of P36 is just put on the standard model (SM) prediction. However, if our result agrees with the current world average which is nearly the result of NA62, it would indicate a deviation of the new world average of about two-sigma from the standard model prediction.

## References

- [1] the P36 experimental proposal, TREK homepage, <http://trek.kek.jp/e36/proposal/proposal.pdf>.
- [2] an Addendum to the P36 experimental proposal, TREK homepage, <http://trek.kek.jp/e36/proposal/addendum1.pdf>
- [3] C. Lazzeroni et al., Phys. Lett. **B698** (2011) 105; E. Goudzovski et al., in proceedings of PANIC2011, arXiv:hep-ex/1111.2818.
- [4] F. Ambrosino et al., Eur. Phys. J. C64 (2009) 627; Erratum-ibid. C65 (2010) 703.
- [5] S. Shimizu et al., Phys. Lett. **B495** (2000) 33.
- [6] K. Horie et al., Phys. Lett. **B513** (2001) 311.
- [7] M.A. Aliev et al., Phys. Lett. **B554** (2003) 7; M.A. Aliev et al., Eur. Phys. J. **46** (2006) 61.
- [8] S. Shimizu et al., Phys. Rev. **D70** (2004) 037101.
- [9] S. Shimizu et al., Phys. Lett. **B633** (2006) 190.
- [10] J. Bijmens, G. Colangelo, G. Ecker, J. Gasser, arXiv:hep-ph/ 9411311. Published in 2nd DAPHNE Physics Handbook:315-389
- [11] C.H. Chen, C.Q. Geng, C.C. Lih, Phys. Rev. D 77, 014004 (2008)
- [12] C. Gatti, Eur. Phys. J. **C45** (2006) 417.
- [13] S. Weinberg, Phys. Rev. **140**, 516 (1965)
- [14] TREK homepage, <http://trek.kek.jp/>
- [15] An 800 MeV/c separated kaon beam at J-PARC, J. Doornbos, April 2005.
- [16] Review of Particle physics, Particle Data Group, <http://pdg.lbl.gov/>